HAL
open science

# Crustal structure of the Gulf of Aden southern margin: Evidence from receiver functions on Socotra Island (Yemen)

Abdulhakim Ahmed, Sylvie Leroy, Derek Keir, Félicie Korostelev, Khaled Khanbari, Frédérique Rolandone, Graham Stuart, Mathias Obrebski

## To cite this version:

Abdulhakim Ahmed, Sylvie Leroy, Derek Keir, Félicie Korostelev, Khaled Khanbari, et al.. Crustal structure of the Gulf of Aden southern margin: Evidence from receiver functions on Socotra Island (Yemen). Tectonophysics, 2014, pp.1-17. 10.1016/j.tecto.2014.10.014 . hal-01081670

**HAL Id: hal-01081670**

**https://hal.science/hal-01081670**

Submitted on 10 Nov 2014

**HAL** is a multi-disciplinary open access archive for the deposit and dissemination of scientific research documents, whether they are published or not. The documents may come from teaching and research institutions in France or abroad, or from public or private research centers.

L'archive ouverte pluridisciplinaire **HAL**, est destinée au dépôt et à la diffusion de documents scientifiques de niveau recherche, publiés ou non, émanant des établissements d'enseignement et de recherche français ou étrangers, des laboratoires publics ou privés.

# Crustal structure of the Gulf of Aden southern margin: Evidence from receiver functions on Socotra Island (Yemen)

**Abdulhakim Ahmed[1,2,3], Sylvie Leroy,[1,2]*, Derek Keir[4], , Félicie Korostelev[1,2], Khaled Khanbari[5,6] , Frédérique Rolandone[1,2], Graham Stuart[7], Mathias Obrebski[8]**

1 *Sorbonne Universités, UPMC Univ Paris 06, UMR 7193, Institut des Sciences de la Terre Paris (iSTeP), F-75005 Paris, France*

2 *CNRS/INSU, UMR 7193, Institut des Sciences de la Terre Paris (iSTeP), F-75005 Paris, France*

3 Seismological and Volcanological Observatory Center, Dhamar, Yemen.

4 National Oceanography Centre Southampton, University of Southampton, Southampton, United Kingdom, SO14 3ZH, UK.

5 Yemen Remote Sensing Center and Dep. of Earth & Environmental Science

6 Sana'a University Yemen

7 School of Earth and Environment, University of Leeds, Leeds, UK.

8 Lamont-Doherty Earth Observatory, University of Columbia, NY.

** corresponding author: Tel: +33144273408 Fax: +33144274950; email: sylvie.leroy@upmc.fr*

## Abstract

Breakup of continents in magma-poor setting occurs primarily by faulting and plate thinning. Spatial and temporal variations in these processes can be influenced by the pre-rift basement structure as well as by early syn-rift segmentation of the rift. In order to better understand crustal deformation and influence of pre-rift architecture on breakup we use receiver functions from teleseismic recordings from Socotra which is part of the subaerial Oligo-Miocene age southern margin of the Gulf of Aden. We determine variations in crustal thickness and elastic properties, from which we interpret the degree of extension related thinning and crustal composition. Our computed receiver functions show an average crustal thickness of ~28km for central Socotra, which decreases westward along the margin to an average of ~21km. In addition, the crust thins with proximity to the continent–ocean transition to ~16 km in the northwest. Assuming an initial pre-rift crustal thickness of 35km (undeformed Arabian plate), we estimate a stretching factor in the range of ~2.1-2.4 beneath Socotra. Our results show considerable differences between the crustal structure of Socotra's eastern and western sides on either side of the Hadibo Transfer Zone; the east displays a clear intracrustal conversion phase and thick crust when compared with the western part. The majority of measurements across Socotra

show Vp/Vs ratios of between 1.70-1.77 and are broadly consistent with the Vp/Vs values expected from the granitic and carbonate rock type exposed at the surface. Our results strongly suggest that intrusion of mafic rock is absent or minimal, providing evidence that mechanical thinning accommodated the majority of crustal extension. From our observations we interpret that the western part of Socotra corresponds to the necking zone of a classic magma-poor continental margin, while the eastern part corresponds to the proximal domain.

***Keywords:*** *Magma-poor Margin; Crustal deformation; margin segmentation; Necking zone; Gulf of Aden; receiver function*

## 1. Introduction

The eastern Gulf of Aden continental margins are magma-poor oblique-rifted margins (Fig. 1a) (Leroy et al 2010a; Bellahsen et al 2013a). As such, long fracture zones generated by transform faults impose a first order control on the along-rift segmentation of the young ocean basin (Leroy et al., 2012; Bellahsen et al 2013b). The Arabian plate is thought to have broken away from the Somalian plate at 20-18 Ma, with the young passive rifted conjugate margins still largely exposed subaerially (d'Acremont et al 2010; Fournier et al 2010). This makes it easy to interpret the extensional and sedimentary processes active during continental breakup. Post-rift sedimentary cover is generally relatively thin (0.5-1 km) (Leroy et al., 2004; d'Acremont et al, 2005) and seismic reflection profiles show an absence of seaward dipping reflectors (d'Acremont et al, 2005; Autin et al 2010; Leroy et al 2010) making syn/post-rift sediment and basement easily identifiable and mappeable. The structure of the margin is therefore interpretable on upper-crustal and crustal scale cross sections (Tiberi et al., 2007; d'Acremont et al., 2005; 2006; 2010; Autin et al., 2010a; Leroy et al., 2004, 2010a, 2012).

Magma-poor rifted margins show a characteristic architecture within three distinct divisions from continent to ocean: the proximal, distal, and ocean-continent transition domains. The proximal domain is characterized by rift-basins bound by high-angle listric faults with limited crustal thinning ($\beta < 2$) (e.g. Mohn et al., 2012). The crust of the distal domain is extremely thin with listric

detachment faults commonly penetrating the whole crust. This differs from the proximal domain where fault do not cut through the whole crust (Whitmarsh et al., 2001; Peron-Pinvidic et al. 2009; Franke, 2013). Mohn et al. (2012) defined a narrow necking zone between proximal and distal domains. Necking of the continental crust occurs in a narrow transition zone from slightly stretched and thinned crust (~30 km) to extremely thinned crust (<10 km) with $\beta > 2$ (Mohn et al., 2012). The ocean-continent transition (OCT) is defined as the domain of exhumed sub-continental mantle (Mohn et al., 2012; Franke, 2013) if it has been sampled. If no samples are available then the OCT is defined as a domain of uncertain affinity between the thinned continental crust and the crust that displays clear oceanic geophysical characteristics (see Leroy et al., 2010a for details). Hence, crustal thickness variation along rifted margins from the proximal domain to the distal domain is a key parameter required to assess structural segmentation and the strain localization during the transition from continental break-up to active oceanic spreading.

During the last few decades, detailed geophysical and geological studies have been carried out within the Gulf of Aden to evaluate the initiation and development of the active spreading ridge (Sheba ridge) (Fig. 1a,b). These studies have provided bathymetric (Leroy et al., 2004), seismic (Laughton et al., 1970; Stein and Cochran, 1985; d'Acremont et al., 2005, 2010; Autin et al., 2010a; Leroy et al., 2004, 2010a,b; Watremez et al., 2011, Bache et al 2011), gravity, magnetic (d'Acremont et al., 2006; Leroy et al., 2010a; Fournier et al., 2010; Leroy et al 2012, Ali and Watts 2013), and heat flow (Lucazeau et al., 2008, 2009, 2010; Rolandone et al 2013) constraints. The interpretation of these data has resulted in a detailed model of the evolution of the eastern Gulf of Aden from rifting to oceanic spreading. In addition to these marine geophysical studies, detailed onshore stratigraphical, geological, structural, and geophysical studies have been carried out on the northern continental margin of the Gulf in eastern Yemen and Oman (Platel and Roger, 1989; Platel et al., 1992; Menzies et al., 1992; 1997; Huchon and Khanbari, 2003; Tiberi et al., 2007; Bellahsen et al., 2006; Basuyau et al., 2010; Al- Hashmi et al., 2011; Chang and Van der Lee, 2011; Al-Lazki et al., 2012; Leroy et al., 2012; Denèle et al 2012; Bellahsen et al., 2013; Robinet et al., 2013; Ahmed et al 2013; Korostelev et al 2014; Corbeau et al

2014). These studies reveal extension directions of N20°E parallel to the plate motion and N160°E perpendicular to the main direction of the oblique rift (Autin et al. 2010b; Brühne and Autin, 2013) and thinning of the crust from a thickness of 35 km at 30 km inland from the coast to a thickness of 26 km at the coast. Unfortunately, it has not been possible to carry out similar studies along the southern margin of the Gulf of Aden, where the surface geology investigation was previously limited to field mapping of the Socotra archipelago (e.g., Beydoun and Bichan, 1969; Samuel et al., 1997; Fournier et al., 2007; Al-Wasaby and Al-Aydrus, 2011; Leroy et al., 2012; Denèle et al., 2012; Bellahsen et al. 2013b; Pik et al. 2013), a shallow marine seismic reflection line on the southern Socotra platform (Birse et al., 1997; Morrison et al., 1997) and field mapping in Somalia (e.g., Brown, 1930; Fantozzi, 1996; Fantozzi and Sgavetti, 1998; Granath, 2001). Socotra island constitutes an important part of the southern margin located at the easternmost part of the Gulf of Aden (Fig. 1b). It documents the full geological and tectonic history of rifting, including a record of the pre-rift continental architecture that existed when it was still attached to Arabia, as well as the complex geological and tectonic syn-rift stage and post-rift geological and tectonic processes (Leroy et al., 2012). These previous studies do not include imaging of the deep crustal structure that is critical to evaluate crustal scale deformation history and evolution during rifting.

With this purpose in mind, the Socotra component of the YOCMAL (Young Conjugate Margins Laboratory) seismic project was conceived and implemented during 2010 - 2012. YOCMAL deployed 24 new broadband seismic stations to supplement the single permanent seismic station to provide data coverage for the entire island of Socotra. We use teleseismic waveform data from our network to quantify for the first time the variation of the crustal thickness and elastic properties of Socotra. This study provides data and interpretation on the evolution of the whole crust of the southern Aden margin. This enables an interpretation of the breakup history in the context of the better-known northern conjugate margin in Oman, leading to an understanding of rift evolution. We use our results beneath Socotra to better understand plate scale deformation and compositional modification thus improving our understanding

of the breakup history of the youngest non-volcanic passive continental margin on Earth.

## 2. Geological and Tectonic setting

Socotra is the largest of four islands (Socotra, Darsah, Samhah and Abd al Kuri) constituting the Socotra Archipelago located east of Somalia and representing the southeastern Gulf of Aden margin. Geographically Socotra is ~380 km south of Ras Fartaq in mainland Yemen and ~250 km east of the Horn of Africa (Fig. 1). The greatest depth to the seafloor surrounding the islands is ~2500 m, north of the archipelago. The ~70km wide Socotra Platform to the south of the islands is at water depths of less than ~250 m. South of the Socotra Platform the seafloor drops to ~5000 m in the North Somali Basin (Birse et al., 1997) (Fig. 1).

The continental rifting which eventually formed the Gulf of Aden conjugate margins began as early as the Oligocene (~34 Ma) with the formation of rift valley grabens (Leroy et al., 2010a; 2012; d'Acremont et al 2005; 2006; 2010; Robinet et al 2013). Beginning in the early Miocene (~17.6 Ma), oblique seafloor spreading with a mean extension direction of N20°E began to separate the two N75°E trending conjugate margins (Leroy et al 2004; Bellahsen et al 2005; d'Acremont et al., 2006, 2010; Leroy et al., 2010a; 2012) (Fig. 1). Continental breakup resulted in distinct eastern and western structural domains of Socotra, separated by the NE-SW striking Hadibo Transfer Zone (HTZ) located through the middle of the island (Fig. 2; Beydoun and Bichan, 1969; Leroy et al., 2012; Bellahsen et al., 2013b). The eastern domain is composed of a single large tilted block dominated by igneous rocks which forms the ~1500 m high Haggier Mountain Range. The western domain is characterized by tilted blocks bound by ~N110°E trending faults (Leroy et al., 2012; Bellahsen et al., 2013b).

The pre-rift geology of Socotra is a neoproterozoic basement and Cretaceous - Eocene carbonates. The Neoproterozoic basement, which is composed of metamorphic, plutonic and volcanic rocks (Denèle et al., 2012), outcrops over more than 30% of the eastern domain in the Haggier Mountains (Fig.2). In the western domain, basement consisting mainly of metamorphic and biotite granite

rocks outcrops at Qalansiya and Sherubrub (Fig. 2). Pre-rift carbonate-dominated Cretaceous strata were deposited uncomformably over the basement, followed by Paleocene/Middle Eocene carbonate shelf deposits (Beydoun and Bichan, 1969; Leroy et al., 2012).

The pre-rift strata were disturbed by the onset of rifting in the early Oligocene, with the regional stratigraphy providing age constraints on the rift history (Leroy et al., 2012). Syn-rift carbonate sediments were deposited in three fault bound Oligocene basins preserved in the western domain of the island (Fig. 2). Of these the Allan- Kadama and Sherubrub-Balan basins are bound by ~N110°E trending low-angle normal faults, and the Central Basin is aligned with the southern part of the HTZ (Bellahsen et al., 2013b) (Fig. 2). The HTZ is a pre-existing structure associated with Permian-Triassic rifting which was reactivated during the opening of the Gulf of Aden (Denèle et al., 2012; Leroy et al., 2012; Bellahsen et al., 2013b). There are no syn-rift sediments on the eastern domain and the spatially limited rift faults are high angle (e.g. in Jebel Haggier) (Fig. 2).

Recent thermochronological dating indicates a slightly younger age of rift development in the eastern Socotra domain (38 ± 2 Ma) compared to the western Socotra domain (32 ± 2 Ma), which suggests that the HTZ was already reactivated at that time (Pik et al., 2013). A second phase of uplift and erosion is recorded only in the strata of the eastern part of the island at 20 ± 2 Ma. This post-dates the onset of rifting, but is synchronous with development of the OCT offshore (Leroy et al., 2010a; Pik et al., 2013). The maximum denudation is close to the HTZ.

Post-rift sediments sealed the rifted-blocks faults activity with dominant vertical movement from the end of the Miocene to the Quaternary. This resulted in deposition of deltaic fans of continent-derived conglomerates in local basins during a major uplift phase (Leroy et al., 2012). This was followed by subsidence and marine deposition on eroded, older pre-rift and syn-rift strata (Beydoun and Bichan, 1969; Leroy et al., 2012).

## 3. Data and methodology

### 3.1 Data

A temporary seismic network of 24 three-component broadband stations in total was installed on Socotra. The network operated for a period of 12 months in two time periods between March 2010 and March 2011 and September 2011 to September 2012 as part of the YOCMAL seismic project. The seismic stations were distributed over the entire island of Socotra with station separation ranging from 5 to 40 km (Fig. 2). Firstly, the seismic network consisted of 6 Güralp CMG-3ESPD (60 s natural period) sensors, 13 Güralp CMG-6TD (30 s natural period) sensors and 2 Güralp CMG-40T (30 s natural period) sensors with RefTek-130 data acquisition systems. Additional data were collected from 3 temporary broadband stations (Fig. 2) equipped with Güralp CMG-40T sensors and RefTek-130 data acquisition systems, operated as an auxiliary part of the YOCMAL seismic project for 12 months between September 2011 and September 2012. In addition, data from one permanent GFZ broadband station SOCY, which was equipped with an STS-2 seismometer and a Quanterra-330 datalogger (shown as triangle in Fig. 2), were analyzed.

The seismic data were continuously sampled at 40 Hz by the temporary seismic stations and at both 100 and 20 Hz by the permanent network. All stations were equipped with GPS timing systems operated in continuous mode to synchronize the stations' internal clocks.

We used 100 teleseismic events with magnitudes >5.5 within an epicentral distance range of 25°-95° from each station (Fig. 1c). The raw waveform data were windowed to start 30s before and ending 30s after the computed IASP91 P-arrival time. We filtered the selected signal with a zero phase Butterworth bandpass filter with corner frequencies of 0.05-0.8 Hz. Based on the signal-to-noise ratio of P-wave phase and disturbances (e.g., spikes, glitches, sensor re-centering, calibration pulses, missing data…etc.) within 30 seconds after the P-wave arrival, we selected the best waveform data recorded at each station. The signal-to-noise ratio of P-wave phase is calculated using $SN=A_s/A_n$, where $A_s$ is the signal Root Mean Square variance in the time window of 2s before and 18s after the P-arrival time, and $A_n$ is the noise Root Mean Square variance in the time window of 22s-2s before the P-arrival time. Events with a signal to noise

ratio (SN) of three or greater on the vertical component were selected and converted to radial and tangential RFs (Ligorria and Ammon, 1999). The RFs then evaluated with careful visual inspection to accept those with a clear positive polarity P-wave arrival at, or shortly after zero time on the radial signal. In addition, accepted RFs have a tangential signal with smaller amplitudes compared to the radial signal and have no significant ringing on the radial or tangential signals.

The number of events used for final analysis at each station varies from 18 to 56 (Table 1), depending on the background noise and the technical state of the station. Most of the selected events have an ENE backazimuth with some events from the south and some from the northwest (Fig. 1c).

### 3.2 Receiver function analysis

The receiver function method maps the seismic discontinuities within the Earth below three-component seismic stations by removing the effects of the source, propagation path and instrument response from the waveform of incident teleseismic P–waves that have been partially converted to S–waves. The amplitudes and polarity of the converted phases are sensitive to the impedance contrasts between the layers above and below the seismic discontinuity. The delayed arrival time of the P–waves converted to S–waves compared to the arrival time of the direct P–wave is a function of P– and S–waves velocities above the seismic discontinuity and the depth of the discontinuity (Fig 3f). Hence, crustal thickness and elastic property information can be derived from receiver function analysis (Vinnik, 1977; Langston, 1977, 1979; 0wens et al., 1984; Zandt et al., 1995).

We employ the iterative time domain deconvolution technique developed by Ligorria and Ammon (1999) to compute the receiver functions. We calculate the receiver function by applying several processing steps. The N-S and E-W horizontal components were rotated to radial and tangential components. A 30 s time window (5 s before the theoretical P arrival time and 25 s after) was used to deconvolve the vertical component from the radial and transverse components. We applied a Gaussian filter of 2.5 to the deconvolved spike wave train, except for the noisiest stations where a Gaussian width of 2.0 is used to smooth the

receiver function (e.g., Ligorria and Ammon, 1999). Fig. (4) and Fig. (S1) shows the individual RFs at each station plotted as a function of backazimuth, and Fig. (3 a-d) shows the stacked receiver functions for all stations.

We adopt the H–k domain stacking technique (Zhu and Kanamori, 2000), to estimate the crustal thickness (H) and the average crustal Vp/Vs ratio (k). Inversion results can be seen in Fig. 5 and Fig. S2. The method sums the receiver function amplitudes of the Moho conversion of P– to S–waves and its multiple converted phases (PpPs and PpSs+PsPs) (Fig. 3f) at predicted arrival times for different crustal thickness (H) and Vp/Vs ratio (k) pairs, transforming them from time domain to H-k domain. This approach assumes an average Vp for the whole crust and the best estimate for the crustal model is achieved with the maximum summation:

$$s(H,k) = \sum_{i=1}^{n} \left[ w_1 r_i(t_{Pms}) + w_2 r_i\left(t_{PpPs}\right) - w_3 r_i\left(t_{PpSs+PsPs}\right) \right] \dots\dots\dots (1($$

Where n is the number of receiver functions, Wj ,(j=1,2,3) is a weighting factor that represents the contribution of the corresponding seismic phase according to signal-to-noise ratio (with the constraint that W1+W2+W3 = 1) and $r_i$(t) is the amplitude of the receiver function at time t of the associated seismic phase. The primary conversion phase that has the highest signal-to-noise ratio is associated with the highest weight. Low weights (W2+W3<W1) are assigned to the multiples (PpPs and PpSs+PsPs) in comparison to the primary phase Pms because the slopes of crustal multiples are very similar in the H-k plane (Zhu and Kanamori, 2000). In case of low signal-to-noise ratio the multiples are down weighted because they are often weak signals and masked by noise. Different values have been tested to evaluate the sensitivity of stacking results to the assigned weight. Then we assign weights of W1=0.6, W2=0.3 and W3=0.1 for the primary phase and multiples, respectively (Zhu and Kanamori, 2000). At a few stations these values have been adjusted based on the visibility of the multiples, using to set of weights W1=0.7, W2=0.2, W3=0.1 and W1=0.8, W2=0.2, W3=0.0.

The theoretical travel times of Pms, PpPs and PpSs+PsPs can be calculated as follows:

$$t_{Pms} = H\left[\sqrt{(V_s^2 - p^2)} - \sqrt{\left(V_p^2 - p^2\right)}\right] \ldots\ldots\ldots\ldots..(2($$

$$t_{PpPs} = H\left[\sqrt{(V_s^2 - p^2)} + \sqrt{\left(V_p^2 - p^2\right)}\right] \ldots\ldots\ldots\ldots.(3($$

$$t_{PpSs+PsPs} = H\left[\sqrt{(V_s^2 - p^2)} - \sqrt{\left(V_p^2 - p^2\right)}\right] \ldots\ldots(4($$

Due to the lack of a-priori velocity information, we tested the H–k technique with a range of average crustal velocities Vp (5.8, 6.0, 6.2, 6.4, 6.6 and 6.8 km/s) to determine the most appropriate average velocity to be used in the inversion for H and k in the different regions of Socotra (an example of the results are shown in the supplementary materials, Fig. S4). We chose a value of 6.4 km/s for average crustal velocity (Vp), in agreement with the global average for continental crust (Christensen and Mooney, 1995) and previous receiver function results in the northern margin of the Gulf of Aden (Tiberi et al., 2007; Ahmed et al., 2013).

A grid search in the 10-40 km interval Moho depth (H) versus 1.6 to 1.9 Vp/Vs ratio (k) is carried out to obtain the maximum stacked amplitude. In the minority of cases, we further limit the searched range of Vp/Vs ratios to avoid unrealistic crustal thickness and/or Vp/Vs results due to some crustal reverberations in the receiver function signal. We show the range of searched k values appear in the H-k diagrams.

We use the bootstrap resampling technique (Efron and Tibshirani, 1986) to estimate the errors of Moho depth and Vp/Vs ratio. The technique randomly samples subsets of receiver functions available for each station, recalculating the Moho depth and Vp/Vs ratio using the Zhu & Kanamori (2000) stacking method. This resampling is repeated 200 times and the standard deviation of these 200 results gives the error estimates for the stacking method and is displayed as error bars in the depth sections. We also use a bootstrap analysis to estimate the errors due to the sensitivity of the method to the assumed Vp value. For each

station, we recalculate H and Vp/Vs for 200 randomly chosen values of Vp within the range 5.8 kms-1 – 6.8 kms-1 (Tiberi et al., 2007). Results of error estimates are shown in the supplementary material (Fig. S4).

To determine the velocity model of a layered crust that matches our RF results at selected sites of eastern and western domains of Socotra, we perform RF inversion with a stochastic method (Shibutani et al., 1996). The stacked radial receiver functions of each station are inverted for 1-D shear wave velocity structure using the Neighborhood Algorithm (NA) technique (Sambridge, 1999a, 1999b). The initial model is based on the results of previous geophysical studies of the crustal structure beneath the Arabian plate on the northern conjugate margin (e.g., Mooney et al., 1985; Al-Amri et al., 1998, 1999), and the Vp/Vs ratio is estimated from H–k stacking results. The model parameters are the thickness of the layer, the shear wave velocity at the top and bottom of each layer, the Vp/Vs ratio and the density. Our starting model is composed of 4 to 5 layers: sediment layer when needed, basement, upper crust, lower crust and uppermost mantle. Shear wave velocity construction at each layer and the computation of the synthetic waveforms follow the method implemented by Shibutani et al. (1996).

## 4. Results

Moho depth H and Vp/Vs results from receiver functions analysis are shown on the geological map of Socotra island Fig. (6a) and Fig. (6b) respectively. The Pms Moho conversion phase appears clearly at all the stations from individual and stacked receiver functions (Fig. 3 and 4). Multiples (PpPs+PsSs) are clearly observed in the majority of stacked receiver functions, however, the Moho multiples may be disturbed by multiples from intracrustal and/or upper mantle interfaces at some stations (Fig. 4). Calculated crustal thickness and Vp/Vs ratio with uncertainties are compiled in Table 1. We organize the results into the eastern and western domains separated by the HTZ, on the basis of their differing geology and also in light of contrasting crustal properties found in our new study (Fig. 2). Most of the stations in the eastern domain display a clear intracrustal conversion phase and thick crust, contrasting the western domain which has thin crust and the absence of strong intracrustal discontinuities.

### 4.1 Eastern Socotra

With the exception of SAYH station, clear positive intracrustal phases are observed within 1.23-1.82 s of the direct P-wave arrival. At some stations (e.g., DESH, HEIL and GSFO) these phases are associated with crustal multiples (PpPs+PsSs) within 5-10 s after the direct P–wave arrival. In all the individual (Fig. 4) as well as stacked receiver functions from all the eastern stations (Fig. 3), a strong positive conversion phase arrives within a delay time of 3.1-3.8 s after the P–wave arrival. These conversions indicate a seismic velocity discontinuity that increases with depth and is interpreted as the Moho discontinuity.

The H–k stacking results (Fig. 6 a, b) indicate that the crustal thickness beneath eastern stations increases westward from 22.4 ± 0.6 km (SAYH) to its maximum value of 30.2 ± 1.1 km beneath BIRZ station on the plateau near the HTZ (Fig. 2). The associated Vp/Vs values for the eastern stations range from 1.70 (HEIL) located on the basement rock east of Hadibo to 1.82 (SAYH) located on sedimentary rock at the eastern part of the island. A very high value of 1.94 is estimated for TROB located near HTZ at the northern base of Haggier Mountain (Fig. 6b). The positive phase that arrives before the Moho conversion phase can be attributed to an intracrustal discontinuity located at a depth range of 10-16 km depending on the selected average velocity.

### 4.2 Western Socotra Island

The crustal thickness of the western domain of the island increases from the NNW to SSE, such that the western part can be divided into EW-trending zones with uniform crustal thickness. These zones broadly correlate with the three Oligocene basins (from north to south being the Allan- Kadama, Sherubrub-Balan, and Central basins) The northernmost zone, located on the northwest coast of the island, is narrow with a Moho Pms conversion phase of 2 to 2.5 s after the first P–wave arrival and multiples within a 7-10.5 s delay (Fig. 2 and 3). The corresponding crustal thickness in this zone is estimated at 16.4 km (RUSU) and 16.8 km (KADA) (Figs 5 and S1-2). To the south in and around the Sherubrub-Balan basin five stations are characterized by a clear Moho conversion phase that arrives with a delay of 2.3-3.1 s after the arrival of the

direct P phase. This zone, with an estimated crustal thickness of 19.6-21.6 km, makes up a large part of the western end of the island, mainly below Jebel Mala, Jebel Zala, and Jebel Allan, and on the coast at the SHRQ station (Figs. 2, 6a, and 8). Seven stations were located on the third E-W zone at the middle part of western Socotra between Sherubrub (SHER) on the coast and LISK station to the east (Figs 2 and 8). It is characterized by Moho conversions that arrive within a time window of 2.67 to 3.17 s with associated depth ranges of 20.2 to 23.4 km. In our third, southernmost zone of the Central Basin, four stations constrain the crustal thickness to range between 26.4 and 28.2 km. Here the Moho conversion phase Pms delay time is of 3.5-3.7 s and multiples arrive 11.3-15.3 s after the first of P– wave arrival (Figs. 2, 6a, and 8).

The average value of the Vp/Vs ratio in the western domain of the island is ~1.75. Lower Vp/Vs ratios (1.65-1.71) are observed beneath some stations, which are located on or near granitic bodies (RUSU, DIAA and SHER) (Fig. 6b). Higher Vp/Vs ratios of 1.77-1.84 are obtained for the stations located in the Sherubrub-Balan basin (RIGI, AMAD, SHUA, HAME, MDAP, LISK and SHRQ) and also beneath DANA station near the southern coast. A high value of 1.89 is observed for the station located near the northern coast of the western domain (KADA) (Fig. 6b).

### 4.3 Migrated cross sections

The migrated cross sections obtained from two ~N-S profiles in the western domain of the island and two E-W profiles across the entire island are presented in Fig. 8. We utilized the IASP91 velocity-depth reference model (Kennett and Engdahl, 1991) to migrate the receiver functions from time domain to space domain, using the common conversion point (CCP) stacking technique of Dueker and Sheehan (1997) and of Zhu (2000). A bin size of 10 km width, 3 km length and 0.5 km depth is used.

The positive amplitudes, which indicate an increase of velocity with depth, are plotted in red, while negative amplitudes are shown in blue. Profile A-B, which is located at the westernmost part of the island, runs from Sherubrub on the southern coast to Kadama on the northern coast (Fig. 8b). The Moho discontinuity occurs at ~23 km beneath the southern end of profile A-B and then

ascends to ~17 km beneath the northern end. The area located below KADA, RUSU and DIAA stations where the crust thins to ~16 km shows some energy placed between the surface and Moho (Yellow-Orange colors), which may indicate a rather uniform high velocity gradient extending from the surface to the Moho underneath MALA, DIAA and RUSU stations (Fig. 8a). Another feature present near the northern end of this profile is a localized upper mantle discontinuity at 43 km depth (Fig. 8a). Profile C-D, which is located ~17 km to the east of and approximately parallel to Profile A-B, extends from DANA station located on the southern coast to SHRQ station on the northern coast. The Moho depth decreases gently from ~26 km in the south (DANA and WURE) to ~20 km near the north coast (Fig. 8b).

The distribution of stations is sparser to the east along the E-W profiles. Profile E-F extends from SAYH station in the west of Ras Momi (eastern domain) to SHER station located at Sherubrub (western domain) (Fig. 8). The Moho depth is approximately equal at the two ends of the profile (~22 km) and increases to its maximum below the Haggier Mountains and plateau (Fig. 8c). Profile G-H runs parallel to the northern coast of the island from SAYH station in the west of Ras Momi (eastern domain) to MALA station located in the south of Qalansiya (western domain)(Fig. 8). Along this profile, the Moho depth increases from ~22 km at the eastern end to a ~28 km below Haggier mountains and then shallows to ~16 km at its western end below the stations located near Qalansiya (Figs 7 and 8d). The isolated upper mantle interface at ~43 km depth below the western domain, which has been observed in the profile A-B, can also be seen on this profile. In addition we observe a constant velocity gradient that extends from the surface down to Moho below the stations located NE of Qalansiya (MALA, DIAA and RUSU) (Fig. 8d).

In the eastern part of the G-H and E-F profiles a clear positive phase is observed indicating velocity increase downward. It corresponds to a strong crustal convertor at all the eastern stations, with the exception of SAYH where it is weak and smeared. The positive phase is imaged at approximately 10 km depth and we interpret it to be mid-crustal interface between the upper and lower crust. A vertical step of about 2 km is observed near the location of HTZ and also imaged very clearly along the G-H section.

To further our understanding of the crustal structure beneath the stations in both eastern and western domains that our RFs and migrated cross sections show an intracrustal feature, we inverted the receiver function waveforms for SOCY (eastern Socotra) and DIAA (western Socotra) using the NA algorithm (Sambridge, 1999a,b). SOCY has a clear Moho conversion and multiples in addition to an intracrustal phase and thick crust (see CCP images Fig. 8c,d and RFs stacks Fig. 3a). In contrast DIAA, located in the Qalansiya Valley shows a thin crust, and the velocity increases with depth continuously rather than in discrete steps (see CCP images Fig. 8a,d). These two stations are also characterized by many events with representative RF's.

To further our understanding of the crustal structure underneath the stations in both eastern and western domains that shows an intracrustal feature in the RFs and in the migrated cross sections, we inverted the receiver function waveforms for SOCY (eastern Socotra) and DIAA (western Socotra) using the NA algorithm (Sambridge, 1999a,b). SOCY has a clear Moho conversion and multiples in addition to an intracrustal phase and thick crust (see CCP images Fig. 8c,d and RFs stacks Fig. 3a), while at DIAA, located in the Qalansiya Valley with a thin crust, the velocity increases with depth continuously rather than in discrete steps (see CCP images Fig. 8a,d). These two stations are also characterized by many events with representative RF's. Examples of inversion results are shown in Fig. 9. We obtain crustal thicknesses comparable to those obtained using the technique of Zhu and Kanamori (2000) (Figs 4 and 5).

## 5. Discussion

### *5.1 Distinct crustal thinning on either side of a fracture zone*

#### *5.1.1 Eastern Socotra*

Our crustal thickness estimates for eastern Socotra range from 27.6 km (GSFO) to 30.2 km (BIRZ) with an average of 28.6 km below the Haggier massif and 22.4-23.6 km with an average of 23.0 km to the east of the Haggier massif. Our results for the Haggier massif are very close to the crustal thickness (29.2 km) found for the southern Omani coast near Mirbat that represents the conjugate margin of the Socotra area (Tiberi et al., 2007). The crustal thinning from ~28.6 km below

Haggier massif to 23 km at the easternmost part of the island occurs over ~15 km distance between HEIL/GSFO and DESH stations (Fig. 6a). Assuming a 28.6 km thick crust prior to rifting we estimate a stretching factor, β, of ~1.24. This represents a lower bound estimate for total crustal stretching since 28.6 km thickness is likely to be representative of crust that has been thinned during early rifting. If we assume that the unstretched crustal thickness of the Arabian platform and/or Arabian shield on the northern conjugate margin is in the range of 35-40 km (Al- Damegh et al., 2005; Tiberi et al., 2007; Hansen et al., 2007; Al-Hashmi et al 2011; Ahmed et al., 2013) and that 23 km represents the final stretched crustal thickness, then β ranges from 1.52 to 1.74. These values are comparable to the stretching factor obtained for the northern conjugate margins studied in southern Oman and southwestern Yemen (Tiberi et al., 2007; Ahmed et al., 2013). No clear N-S change in crustal thickness and inferred degree of extension is apparent at the eastern Socotra based on the crustal thickness distribution for the stations located on the Haggier massif and close to the HTZ (ca. 28.5±0.9 km). The only clear indication of crustal thinning occurs at DESH and SAYH stations towards the east in the Momi transfer zone area (Fig. 2 and Fig. 8c,d).

For all the stations located on or near the Haggier massif a clear mid-crustal interface occurs at depths between 10-12 km along the E-W profiles (Fig. 3). This interface appears on both profiles, but most clearly on profile G-H along the northern coast (Fig. 8d). Moreover, there is a clear vertical step in the depth to this interface from ~10 km in the east to ~12 km to the west in the vicinity of the HTZ. This interface is not imaged by the receiver functions west of the HTZ and the easternmost station SAYH. We interpret this interface to be the upper/lower crust boundary also known as the Conrad discontinuity. This discontinuity represents a sharp velocity step separating the upper crust (average Vp of 6.3 km/s) from the lower crust (average Vp of 7.0 km/s) (e.g., Mooney et al., 1985; Ahmed et al., 2013). Such an interface is a common feature in the Arabian plate (Mooney et al., 1985; Egloff et al., 1991; Stern and Johnson, 2010). Stern and Johnson (2010) suggest that it separates slower felsic upper crust from faster mafic lower crust, and may coincide with the transition from brittle to ductile deformation. A similar mid-crustal discontinuity has been reported in at least

seven locations along the northern conjugate margin in southern Oman (Tiberi et al., 2007), below ASH station northern Oman (Al-Hashmi et al., 2011), and in western Yemen (Ahmed et al., 2013) towards the centre of the rift axis. It disappears towards the southern edge of the syn-rift Ashawq graben on the southern coast of Oman (Tiberi et al., 2007).

Our results indicate a ~2 km vertical offset of the intracrustal discontinuity on a westward dipping plane in the vicinity of the HTZ. This feature could be related to in depth displacement across a fault zone of 10 km wide. This fault zone could belong to the HTZ which is interpreted as a dextral N050°E-N070°E transform fault (Fournier et al 2007; Denèle et al 2012; Leroy et al., 2012; Bellahsen et al 2013b, Pik et al 2013). Contrary to Fournier et al. (2007) who concluded that the HTZ was a pre-existing shallow NE-SW fracture zone within the basement, our findings of the vertical shift of Conrad discontinuity across the structure indicates that the HTZ crosscuts the Haggier massif at its western side from the surface down to the lower crust. Moreover, both the Haggier massif and HTZ are pre- existing structures inherited from early history of the margin and are less affected by the Oligo-Miocene rifting episode (Denele et al 2012; Leroy et al., 2012; Bellahsen et al 2013b; Pik et al 2013).

### *5.1.2 Western Socotra Island*

Receiver functions from stations located on the western domain of the island (Fig. 10) do not image the Conrad discontinuity. This may be caused by the crust having been strongly affected by the Oligo-Miocene rifting. Interpretation of the ENCENS cruise seismic profiles at the northern Gulf of Aden margin (Ashwaq-Salalah, Taqah and Mirbat) indicates a gradual velocity increase within the continental domain from 6.0 km/s (upper crustal velocity) to 7.0 km/s (lower crust velocity) without any velocity step (Leroy et al., 2010a). This may indicate that the extensive thinning of the crust is accompanied by removal of the upper crust and/or modification of the crustal composition. Thinning of the crust in the western domain of the island occurred by a similar mechanism of dip slip along detachment faults dividing the western domain into four different areas of uniform E-W and variable N-S crustal thickness. Leroy et al. (2012), based on recent accurate field mapping of Socotra island (Razin et al 2010), described two

complex tilted blocks where previously Fournier et al. (2007) described three tilted blocks. The first block is located along the north-west coast with the low-angle fault bounding the southern side of the ~15-km long, 5-km wide Allan-Kadama basin (Fig. 6). The two stations located in this area provide an estimated average crustal thickness of ~16.5 km, which is the thinnest crust we observe along the southern margin of the Gulf of Aden. This result is consistent with 15-16 km thick continental crust obtained from gravity and seismic data at the southern end of a NE-SW profile along the Gulf of Aden to the west of the study area (d'Acremont et al., 2006) (Fig. 10).

The crustal thickness increases by 5 km away from the OCT over a horizontal distance of ~5 km from the stations in the Allan-Kadama basin to stations in the north of the Sherubrub-Balan basin (Fig. 7). Then it increases slightly over a distance of ~15 km from an average thickness of ~21 km in this second zone to ~23.0 km in a third zone within the Sherubrub-Balan basin. In the fourth zone in the Central basin, located at the southernmost western part of the island and furthest from the OCT, the average crustal thickness is ~26.0 km (Fig. 7). The average crustal thickness in the fourth zone is comparable to the average crustal thickness reported for the southern Omani coast in the Dhofar region (Tiberi et al., 2007) (Fig. 10). Approximately the same stretching factor, β, of 1.1 occurs between the second, third, fourth zones and Mount Haggier, but it is higher ($\beta \approx 1.27$) between the first and second zones. If we assume the initial crustal thickness is the same as the average for the Haggier massif (~28.6 km), and a final crustal thickness is ~16.5 km in the first block, then $\beta \approx 1.7$. Based upon our results for the final crustal thickness at the northwestern part of the Socotra island and assuming an initial crustal thickness of ~35-40 km (Arabian shield and platform; Al-Damegh et al., 2005; Tiberi et al., 2007; Ahmed et al., 2013) the northernmost part of Socotra island has been stretched in the NE-NNE direction by a β factor of ~2.12-2.42.

Although rifted margins show a large variability in their tectonic and sedimentary evolution related to their specific rift history and the presence of pre-existing structures, most rifted margins worldwide share a remarkably comparable large-scale architecture (Fig. 11) (Mohn et al., 2012). Based on the variations of crustal thickness and tectono-stratigraphic structure, eastern

Socotra island appears to belong to the proximal margin and western Socotra to the necking zone as described by Mohn et al. (2012). The eastern domain consists of one large block tilted toward the south, with a large fault at the foot of Mount Haggier dipping toward the north on which there is at least 200 m of throw (Fig. 7 and Fig. 17 of Leroy et al., 2012). The western domain is composed of two tilted blocks with low-angle faults dipping 18° to the north. This configuration could represent the necking zone similar to that observed in the West Iberia margin (Manatschal and Peron-Pinvidic, 2008), in the offshore Aden margin (Leroy et al., 2010a) and in an outcropping margin within an orogen such as in the Alps (Mohn et al., 2012). The uniqueness of the Gulf of Aden margin is that the necking zone, which is typically hundreds of meters below water, outcrops above sea level at Socotra.

*5.2 Vp/Vs ratio and crustal composition*

The spatial distribution of Vp/Vs ratios correlates well with that broadly expected from the mapped rock outcrops on the island (Fig. 6b). Metamorphic basement and granitic intrusions produce low values ($1.65 \leq Vp/Vs \leq 1.71$) and sedimentary and volcanic geological units produce velocities that correspond to felsic to intermediate compositions ($1.73 \leq Vp/Vs \leq 1.84$) (Fig. 6b) (e.g. Christensen and Mooney, 1995; Thompson et el., 2010; Hammond et al., 2011). The Vp/Vs values have no obvious relationships with either crustal thickness or age of the surface rocks (Fig. 6ab).

Five of our stations are located on or near metamorphic basement and granitic intrusions of Haggier massif, Qalansiya and Sherubrub (Figs 2 and 6). The lowest value of 1.65 found at DIAA station, located in the Qalansiya Valley, may be related to the high silica content of paragneisses and quartzites that form the metamorphic basement (Denele et al., 2012). The other four stations (SHER, MALA, RUSU and DESH) are characterized by Vp/Vs values of 1.7-1.71, which are consistent with felsic composition of underlying rock units (Fig. 6b). On the northern conjugate margin in Dhofar-Oman very low Vp/Vs values were found at S09 station located on the metamorphic basement near Mirbat (Tiberi et al., 2007) and in western Yemen a Vp/Vs value of (~1.68) was reported for the

stations located on granitic intrusions or on Precambrian quartz-rich rocks (Ahmed et al., 2013).

Results from thirteen stations, located within the sedimentary basins of the western domain of the island are characterized by a low Vp/Vs value of ~1.73 for the stations located on a thin sedimentary cover (mostly limestone) and a higher value of ~1.83-1.84 for the stations located on a thick sedimentary cover near the middle of the basin. Similarly, in the eastern domain of Socotra, five stations located on the sedimentary cover and at or near the volcanic rocks are characterized by Vp/Vs ratios in the range 1.73-1.82. In general our finding of average Vp/Vs ratio of ~1.7 for stations located at or near silica-rich rock units and average Vp/Vs values of ~1.77 for stations located on the sedimentary cover are consistent with the felsic and intermediate crustal composition (Christensen, 1996; Gallacher et al., 2011; De Plaen et al., 2014). Broadly our Vp/Vs ratios contrast with those at the volcanic rifted western Gulf of Aden continental margin where Vp/Vs is generally 1.8 (Ahmed et al., 2013). Our results of low Vp/Vs shows that the crust has experienced minimal intrusion of mafic rock during breakup, an interpretation consistent with the lack of mafic intrusions and basaltic flows observed at he surface.

The last two stations KADA and TROB are associated with very high Vp/Vs ratios of 1.89 and 1.94 respectively (Fig. 6b). TROB station is located within the complex structure of the HTZ (Leroy et al., 2012; Bellahsen et al., 2013b; Pik et al., 2013) showing the dipping interfaces and step of the mid-crustal interface (Fig. 8d). Hence, P-wave downdip travelling multiples generated at the dipping mid-crustal interface interfere with the Moho multiples and give a poorly constrained Vp/Vs ratio which may overestimate the real value of Vp/Vs ratio beneath the station (Wang et al., 2010). In contrast, the individual receiver functions from KADA are characterized by a clear Pms converted phase and good multiples. In addition the waves approach the station in the up-dip direction that has little effect on the estimate of the Vp/Vs ratio (Wang et al., 2010). The high Vp/Vs associated with the thin crust (~16km) may be due to a more mafic crust with magmatic intrusion near the OCT as in the northern margin (Watremez et al., 2011; Watremez et al., 2013).

**Conclusion**

Receiver functions analyzed in Socotra allow us to map Moho depth and Vp/Vs variations along the southern Gulf of Aden margin. Variability of crustal properties yield a good correlation with tectonic structures of Socotra. 25 crustal thickness (H) and Vp/Vs ratio measurements obtained by using the H–κ stacking technique of Zhu and Kanamori (2000) show that:

- The crust of Socotra island is divided into distinct eastern and western domains. The eastern domain is characterized by an average of 28 km thick crust and pre-existing structures that date from the region's early pre-rift history. The western domain is characterized by an average of 21 km thick crust that was modified during the Oligo-Miocene rifting that led to the opening of the Gulf of Aden. The two parts are separated by the HTZ, a westward dipping plane that may extend to the lower crust.
- In the western domain, rifting resulted in progressive crustal thinning from 26 km in the south to 16.4 km in the north of the island. Four structurally distinct E-W trending areas of average crustal thicknesses of 16.5, 21, 23 and 26 km are defined.
- Assuming the initial crustal thickness of 28.6 km, the maximum currently observed below Socotra, and thinnest crustal thickness of 16.5 km, we estimate a lower bound stretching factor of 1.7. However, a higher stretching factor in the range of ~2.1-2.4 is obtained by assuming the initial crustal thickness more compatible with an undeformed continent such as that found for the Arabian plate (35km).
- An uppermost mantle reflector beneath the anomalously thin crust in the northernmost part of the island has been imaged by our computed receiver functions, but evidence for removal of lower crust and/or underplating could not be assessed with our dataset.
- We computed Vp/Vs to vary between 1.7 and 1.77 at the majority of the stations. This is consistent with a felsic to intermediate crust beneath the stations located at the regions of granite intrusion or at sedimentary basin. The highest Vp/Vs ratios ranging between 1.78-1.84 are mainly associated with sediments. Broadly, the low Vp/Vs ratios are consistent with no or very low volume intrusion of mafic rock into the OCT during

breakup, and therefore suggests magma intrusion did not accommodate significant extension during the breakup of the eastern Gulf of Aden.

- From our observations we propose that the western part of Socotra corresponds to the necking zone of a classic magma-poor continental margin, while the eastern part corresponds to the proximal domain.

## Acknowledgments

We gratefully acknowledge Alex Brisbourne, Victoria Lane and David Hawthorn (NERC Seis-UK equipment pool), the French Embassy in Yemen (J. G. Sarkis, J. Dechezlepretre and C. Bousquet), local governers and the people of the Yemen governerates for their help during the field work. We deeply thank Dr I. Al Ganad from GSMRB during the deployment. We thank C. Tiberi, J. Vergne, G Hetenyi for providing software. The work was funded by the Agency National de la Recherche ANR-07-BLAN-0135 YOCMAL project and Rift2ridge project, CNRS-INSU-PICS Yemen, GSMRB Yemen and Actions Marges. The facilities of SEIS-UK are supported by the Natural Environment Research Council (NERC) under Agreement R8/H10/64. DK is supported by NERC grant NE/L013932/1.

## References

Ahmed, A., Tiberi, C., Leroy, S., Stuart, G.W., Keir, D., Sholan, J., Khanbari, K., Al-Ganad, I. and Basuyau, C., 2013. Crustal structure of the rifted volcanic margins and uplifted plateau of Western Yemen from receiver function analysis. Geophys. J. Int. doi:10.1093/gji/ggt072.

Al-Amri, A., 1998. The crustal structure of the Western Arabian platform from the spectral analysis of long-period P-wave amplitude ratios, Tectonophys., 290, 271–283.

Al-Amri, A., 1999. The crustal and upper-mantle structure of the interior Arabian platform, Geophys. J. Int., 136, 421–430.

Al-Damegh, K., Sandoval, E. and Brazangi, M., 2005. Crustal structure of the Arabian plate: new constraints from the analysis of teleseismic receiver functions. Earth Planet. Sci. Lett., 231, 177–196.

Ali, M.Y., Watts, A.B., 2013. Subsidence history, crustal structure, and evolution

of the Somaliland-Yemen conjugate margin. Journal of Geophysical Research: Solid Earth 118, 1638-1649.

Al-Lazki, A., Ebinger, C., Kendall, M., Helffrich, G., Leroy, S., Tiberi, C., Stuart, G. and Al-Toobi, K., 2012. Upper mantle anisotropy of southeast Arabia passive margin [Gulf of Aden northern conjugate margin], Oman. Arabian Journal of Geosciences 5 (5): 925-934. doi:10.1007/s12517-011-0477-2.

Al-Hashmi, S., Gok, R., Al-Toubi, K., Al-Shijbi, Y., El-Hussain, I., Rodgers, A.J., 2011. Seismic velocity structure at the southeastern margin of the Arabian Peninsula. Geophysical Journal International. http://dx.doi.org/10.1111/j.1365-246X.2011.05067.x

Autin, J., Leroy, S., Beslier, M. O., d'Acremont, E., Razin, P., Ribodetti, A., Bellahsen, N., Robin, C. and Al-Toubi, K., 2010a. Continental break-up history of a deep magma-poor margin from seismic reflection data (northeastern Gulf of Aden margin, offshore Oman). Geophys. J. Int., 180, 501-519.

Autin, J., Bellahsen, N., Husson, L., Beslier, M.O, Leroy, S. and d'Acremont, E. 2010b. Analogue models of oblique rifting in a cold lithosphere. Tectonics, 29, TC6016.

Bache, F., Leroy, S., Baurion, C., Robinet, J., Gorini, C., Lucazeau, F., Razin, P., d'Acremont, E., Al-Toubi, K., 2011. Post-rift uplift of the Dhofar margin (Gulf of Aden). Terra Nova, 23, 10.1111/j.1365-3121.2010.00975.x, 11-18.

Basuyau, C., Tiberi, C., Leroy, S., Stuart, G., Al-Lazki, A., Al-Toubi, K. and Ebinger, C. 2010. Evidence of partial melting beneath a continental margin: case of Dhofar, in the Northeast Gulf of Aden (Sultanante of Oman). Geophys. J. Int., 180,520-534.

Bellahsen, N., Husson, L., Autin, J., Leroy S., d'Acremont E., 2013a. The effect of thermal weakening and buoyancy forces on rift localization: Field evidences from the Gulf of Aden oblique rifting. Tectonophysics. 607, 80-97.

Bellahsen, N., Leroy S., Autin J., Razin P., d'Acremont E., Sloan H., Pik R., Ahmed A. Khanbari K. 2013b. Pre-existing oblique transfer zones and transfer/transform relationships in continental margins: new insights from the southeastern Gulf of Aden, Socotra Island, Yemen - Tectonophysics. 607, 32-50.

Bellahsen, N., Fournier, M., d'Acremont, E., Leroy, S. and Daniel, J. M., 2006. Fault reactivation and rift localization: northeastern Gulf of Aden margin. Tectonics 25:1–14. doi:10.1029/2004TC001626

Beydoun ZR, Bichan HR (1969) The geology of Socotra Island, Gulf of Aden. Quat J, 125:413–446

Birse, A.C.R., Bott, W.F., Morrison, J. and Samuel, M.A., 1997. The Mesozoic and early Tertiary tectonic evolution of the Socotra area, eastern Gulf of Aden,Yemen, Mar. Pet. Geol., 14, 675 – 684.

Bosworth, B., Huchon, P. and McClay, K., 2005. The Red Sea and Gulf of Aden basins. Journal of African Earth Sciences, v. 43, p. 334–378.

Brown, B.C., 1931. The geology of North-Eastern British Somaliland. Q. J. Geol. Soc. London, 87: 259-280.

Brune, S., Autin, J., 2013. The rift to break-up evolution of the Gulf of Aden: Insights from 3D numerical lithospheric-scale modelling. Tectonophysics 607, 65-79.

Chang, S., and S. Van der Lee (2011), Mantle plumes and associated flow beneath Arabia and East Africa, Earth and Planetary Science Letters, 302 (3-4), 448-454.

Christensen, N. I., 1996. Poisson's ratio and crustal seismology,J. Geophys. Res., 101, 3139–3156, doi:10.1029/95JB03446.

Christensen, N.I. and Mooney, W.D., 1995. Seismic velocity structure and composition of the continental crust: a global view. Journal of Geophysical Research 100, 9761– 9788.

Corbeau J., Rolandone F., Leroy S., Al-Lazki A., Stork A., Keir D., Stuart G., Doubre C., Vergne J., A. Ahmed, Khanbari K. 2014 Uppermost mantle velocity from Pn tomography in the Gulf of Aden - Geosphere. doi:10.1130/ges01052.1

d'Acremont, E., Leroy, S., Beslier, M.O., Bellahsen, N., Fournier, M., Robin, C., Maia, M., and Gente, P., 2005. Structure and evolution of the eastern Gulf of Aden conjugate margins from seismic reflection data. Geophys J Int 160:869–890.

d'Acremont, E., Leroy, S., Maia, M., Patriat, P., Beslier, M.O., Bellahsen, N.,

Fournier and M., Gente, P., 2006. Structure and evolution of the eastern Gulf of Aden: insights from magnetic and gravity data (Encens- Sheba/MD117 cruise). Geophys J. Int 165:786–803.

d'Acremont, E., Leroy, S., Maia, M., Gente, P. and Autin, J., 2010. Volcanism, jump and propagation on the Sheba Ridge, eastern Gulf of Aden: segmentation evolution and implications for accretion processes. Geophys J Int 180:535–551.

Denèle, Y., Leroy, S., Pelleter, E., Pik, R., Talbot, J.Y. and Khanbari, K., 2012. The Cryogenian juvenile Arc formation and successive high-K calc-alkaline plutons intrusion of Socotra Island Yemen. Arabian J. Geosciences, 5(5), 903-924. doi:10.1007/s12517-011-0476-3

De Plaen, R.S.M., Bastow, I.D., Chambers, E.L., Keir, D., Gallacher, R., 2014. The development of magmatism along the Cameroon Volcanic Line: Evidnce from seismicity and seismic anisotropy. J. Geophy. Res., in press.

Dueker, K.G., Sheehan, A.F., 1997. Mantle discontinuity structure from midpoint stacks of converted P to S waves across the Yellowstone hotspot track. Journal of Geophysical Research 102, 8313.

Efron, B. and Tibshirani, R., 1986. The Bootstrap Method for standard errors, confidence intervals, and other measures of statistical accuracy. Statistical Sci., 1, No. 1, 1-35.

Egloff, F., Rihm, R., Makris, J., Izzeldin, Y.A., Bobsien, M., Meier, K., Junge, I., Noman, T. and Warsi, W., 1991. Contrasting structural styles of the eastern and westernmargins of the southern Red Sea: the 1988 SONNE experiment. In: J. Makris, P. Mohr and R. Rihm (Editors), Red Sea: Birth and Early History of a New Oceanic Basin. Tectonophysics, 198, 329-353.

Fantozzi, P. L., 1996. Transition from continental to oceanic rifting in the Gulf of Aden: Structural evidence from field mapping in Somalia and Yemen. Tectonophysics, 259, 285–311, doi:10.1016/0040-1951(95) 00208-1.

Fantozzi, P. L., and Sgavetti, M., 1998. Tectonic and sedimentary evolution of the eastern Gulf of Aden continental margins: New structural and stratigraphic data from Somalia and Yemen, in Sedimentation and Tectonics of Rift Basins: Red Sea-Gulf of Aden, edited by B. H. Purser and D. W. J. Bosence, pp. 56 – 76, CRC Press, Boca Raton, Fla.

Fournier M, Bellahsen N, Fabbri O, Gunnell Y, 2004. Oblique rifting and segmentation of the NE Gulf of Aden passive margin. Geochem Geophys Geosyst 5(11):24

Fournier, M., Huchon, P., Khanbari, K. and Leroy, S., 2007. Asymmetry and segmentation of passive margin in Socotra, Eastern Gulf of Aden, controlled by detachment faults?. Geochem Geophys Geosyst 8 (3):Q03013. doi:03010.01029/02006GC001318

Fournier, M., Chamot-Rooke, N., Petit, C.,Huchon, P., Al-Kathiri, A., Audin, L., Beslier, M.O., d'Acremont, E., Fabbri, O., Fleury, J.M., Khanbari, K., Lepvrier, C., Leroy, S., Maillot, B. and Merkouriev, S., 2010. Arabia-Somalia plate kinematics, evolution of the Aden–Owen–Carlsberg triple junction, and opening of the Gulf of Aden. J Geophys Res 115 (B4):B04102. doi:10.1029/2008jb006257.

Franke, D., 2013. Rifting, lithosphere breakup and volcanism: Comparison of magma-poor and volcanic rifted margins. Marine and Petroleum Geology, 43, 63-87.

Gallacher, R., and Bastow, I.D, 2014. The Development of Magmatism Along the Cameroon Volcanic Line: Evidence from Teleseismic Receiver Functions, Tectonics, 31, TC3018, doi:10.1029/2011TC003028

Granath, J. W., 2001. The Nogal rift of northern Somalia: Gulf of Aden. Reactivation of a Mesozoic rift, in Peri-Tethys Memoir 6: Peri-Tethyan Rifts/ Wrench Basins and Passive Margins, edited by P. A. Ziegler et al., Mem. Mus. Nat. Hist., 186, 511 – 527.

Hammond, J.O.S., Kendall, J.-M., Stuart, G.W., Keir, D., Ebinger, C., Ayele, A., and Belachew, M. 2011. The nature of the crust beneath the Afar triple junction: Evidence from receiver functions. Geochemistry Geophysics Geosystems, 12, Q12004, doi:10.1029/2011GC003738.

Hansen S.E., Rodgers A.J., Schwartz S.Y. and Al-Amri A.M.S., 2007. Imaging ruptured lithosphere beneath the Red Sea and Arabian Peninsula. Earth Planet. Sci. Lett., 259, 256–265.

Huchon, P. and Khanbari, K., 2003. Rotation of the syn-rift stress field of the northern Gulf of Aden margin, Yemen, Tectonophysics, 364, 147 – 166.

Korostelev F., Basuyau C., Leroy S., Tiberi C., Ahmed A., Keir D., Stuart G., Rolandone, F., Al Ganad I., Khanbari K., Boschi L. (2014) - Crustal and upper mantle structure beneath south-western margin of the Arabian Peninsula from teleseismic tomography. Gcubed. doi:10.1002/2014GC005316.

Langston, C. A., 1977. Corvallis, Oregon, crustal and upper mantle structure from teleseismic P and S waves. Bull. Seism. Soc. Am., 67, 713-724.

Langston, C. A., 1979. Structure under Mount Rainier, Washington, inferred from teleseismic body waves, J. Geophys. Res., 84, 4749-4762.

Laughton, A.S., Whitmarsh, R.B. and Jones, M.T., 1970. The evolution of the Gulf of Aden. Philosophical Transactions of the Royal Society of London 267 (Ser. A), 227–266.

Leroy, S., Gente, P., Fournier, M., d'Acremont, E., Patriat, P., Beslier, M.-O., Bellahsen,N., Maia, M., Blais, A., Perrot, J., Al-Kathiri, A., Merkouriev, S., Fleury, J.-M., Ruellan, P.-Y., Lepvrier, C. and Huchon, P., 2004. From rifting to spreading in the eastern Gulf of Aden: a geophysical survey of a young oceanic basin from margin to margin. Terra Nova 16, 185–192.

Leroy, S., Lucazeau, F., d'Acremont, E., Watremez, L., Autin, J., Rouzo, S., Bellahsen, N., Tiberi, C., Ebinger, C., Beslier, M.-O., Perrot, J., Razin, P., Rolandone, F., Sloan, H., Stuart, G., Al-Lazki, A., Al-Toubi, K., Bache, F., Bonneville, A., Goutorbe, B., Huchon, P., Unternehr, P. and Khanbari, K. 2010a. Contrasted styles of rifting in the eastern Gulf of Aden: a combined wide-angle MCS and Heat flow survey. Geochem., Geophys., Geosyst. doi:10.1029/2009GC002963.

Leroy, S., d'Acremont, E., Tiberi, C., Basuyau, C., Autin, J. and Lucazeau, F. 2010b. Recent off-axis volcanism in the eastern Gulf of Aden: implications for plume-ridge interactions. Earth Planet. Sci. Lett., doi:10.1016/j.epsl.2010.02.036, 293, 140-153.

Leroy S., Razin P., Autin J., Bache F., d'Acremont E., Watremez L., Robinet J., Baurion C., Denèle Y., Bellahsen N., Lucazeau F., Rolandone F., Rouzo S., Serra Kiel J., Robin C. et al., 2012. From rifting to oceanic spreading in the Gulf of Aden: a synthesis. Arab J. Geosciences. DOI 10.1007/s12517-011-0475-4.

Ligorria, J. and Ammon, G., 1999. Iterative Deconvolution and Receiver Functions Estimation. Bull. Seism. Soc. Am., Vol. 89, 1395-1400.

Lucazeau, F., Leroy, S., Bonneville, A., Goutorbe, B., Rolandone, F., d'Acremont, E., Watremez, L., Düsünur, D., Tuchais, P., Huchon, P., Bellahsen, N. and Al-Toubi, K., 2008. Persistent thermal activity at the Eastern Gulf of Aden after continental break-up. Nat Geosci 854–858. doi:10.1038/ngeo359

Lucazeau, F., Leroy, S., Autin, J., Bonneville, A., Goutorbe, B., Rolandone, F., d'Acremont, E., Watremez, L., Düsünur, D. and Huchon, P., 2009. Post-rift volcanism and high heat-flow at the ocean–continent transition of the Gulf of Aden. Terra Nova 21(4):285–292

Lucazeau, F., Leroy, S., Rolandone, F., d'Acremont, E., Watremez, L., Bonneville, A., Goutorbe, B., Düsünur, D., 2010. Heat-flow and hydrothermal circulations at the ocean–continent transition of the Eastern Gulf of Aden. Earth Planet Sci Lett 295(3–4):554–570. doi:10.1016/j.epsl.2010.04.039

Menzies M. et al. (1992) The timing of crustal magmatism, uplift and crustal extension-preliminary observations from Yemen. In Magmatism and the causes of continental break-up ( ed. B. Storey et al.); Geol. Soc. Lond. Spec. Publ. 68, 293-304.

Menzies, M., Gallagher, K., Yelland, A., Hurford, A.J., 1997. Volcanic and nonvolcanic rifted margins of the Red Sea and Gulf of Aden; crustal cooling and margin evolution in Yemen. Geochim. Cosmochim. Acta 61 (12), 2511–2527.

Mohn, G., Manatschal, G., Beltrando, M., Masini, E. and Kusznir, N., 2012. Necking of continental crust in magmapoor rifted margins: Evidence from the fossil Alpine Tethys margins. Tectonics, 31, TC1012, doi:10.1029/2011TC002961

Mooney, W.D., Gettings, M.E., Blank, H.R. and Healey, J.H., 1985. Saudi Arabian seismic refraction profile: a traveltime interpretation of crustal and upper mantle structure. Tectonophysics 111, 173–246.

Morrison, J., Birse, A., Samuel, M. A., Richardson, S. M., Harbury, N. and Bott, W. F. , 1997. The Cretaceous sequence stratigraphy of the Socotran platform, the Republic of Yemen. Mar. Pet. Geol., 14, 685–699.

Owens, T. J., Zandt, G. and Taylor, S. R., 1984. Seismic evidence for an ancient

rift beneath the Cumberland Plateau, Tennessee: A detailed analysis of broadband teleseismic P-waveforms. J. Geophys. Res., 89, 7783–7795.

Péron-Pinvidic, G., Manatschal, G., 2008. The final rifting evolution at deep magma-poor passive margins from Iberia-Newfoundland: a new point of view. International Journal of Earth Sciences, doi:10.1007/s00531-00008-00337-00539.

Pik, R., Bellahsen, N., Leroy,S., Denèle, Y., Razin, P., Ahmed, A., Khanbari, K. - Structural control of basement 1 denudation in the course of rift development revealed by low-temperature (U-Th-Sm)/He thermochronology of the Socotra Island basement - southern Gulf of Aden margin.Tectonophysics. 607, 17-31.

Platel, J. P., Roger, J., Peters, T. J., Mercolli, I., Kramers, J. D. and Le Me´tour, J., 1992. Geological map of Salalah, Sultanate of Oman, sheet NE 40-09, scale 1:250,000. Minist. of Pet. and Miner., Dir. Gen. of Miner., Muscat, Sultanate of Oman.

Platel, J.P. and Roger, J., 1989. Evolution dynamique du Dhofar (Sultanat d'Oman) pendant le Crétacé et le Tertiaire en relation avec l'ouverture du Golfe d'Aden. Bull Soc Geol Fr 8(2):253–263

Razin, P., Robin, C., Serra Kiel, J., Bellahsen, N., Leroy, S., Grelaud, C., Robinet, J., 2010. Cenozoic evolution of Socotra Island in relation with the opening of the Gulf of Aden, EGU, Vienna.

Robinet, J., Razin, P., Serra-Kiel, J., Gallardo-Garcia, A., Leroy, S., Roger, J., Grelaud, C., 2013. The Paleogene pre-rift to syn-rift succession in the Dhofar margin (northeastern Gulf of Aden): Stratigraphy and depositional environments. Tectonophysics 607, 1-16.

Rolandone F., Lucazeau F., Leroy S., Mareschal JC, Jorant R., Goutorbe B., Bouquerel H. 2013 - New heat flow measurements in Oman and the thermal state of the Arabian shield and platform. Tectonophysics, 589, 77-89. 10.1016/j.tecto.2012.12.034

Sambridge, M,. 1999a. Geophysical inversion with a neighbourhood algorithm-I. Searching a parameter space. Geophys. J. Int., 138, 479–94.

Sambridge, M., 1999b. Geophysical inversion with a neighbourhood algorithm-

II. Appraising the ensemble. Geophys. J. Int., 138, 727–46.

Shibutani, T., Sambridge, M. and Kennett, B., 1996. Genetic algorithm inversion for receiver functions with application to crust and uppermost mantle structure beneath Eastern Australia. Geophys. Res. Lett. 23(14): doi: 10.1029/96GL01671. issn: 0094-8276.

Stein, C. A. and Cochran, J. R., 1985. The transition between the Sheba ridge and the Owen basin: Rifting of old oceanic lithosphere. Geophys. J. R. Astron. Soc., 81, 47–74.

Stern, R.J., Johnson, P., 2010. Continental lithosphere of the Arabian Plate: a geologic, petrologic, and geophysical synthesis. Earth-Science Reviews 101, 29–67.

Tiberi, C., Leroy, S., d'Acremont, E., Bellahsen, N., Ebinger, C., Al-Lazki, A. and Pointu, A., 2007. Crustal geometry of the northeastern Gulf of Aden passive margin: localization of the deformation inferred from receiver function analysis. Geophys. J. Int., 168(doi:10.1111/j.1365-246X.2006.03294.x): 1247-1260.

Thompson DA**,** Bastow ID, Helffrich G, Kendall J-M, Wookey J, Snyder DB, Eaton DW. 2010. Precambrian Crustal Evolution: Seismic constraints from the Canadian Shield, *Earth and Planetary Science Letters*, **297**,655-666. doi: 10.1016/j.epsl.2010.07.021

Wang, P., L. Wang, N. Mi, J. Liu, H. Li, D. Yu, M. Xu, X. Wang, and Z. Guo (2010), Crustal thickness and average Vp /Vs ratio variations in southwest Yunnan, China, from teleseismic receiver functions, J. Geophys. Res., 115, B11308, doi:10.1029/2009JB006651.

Watremez, L., Leroy, S., Rouzo, S., d'Acremont, E., Unternehr, P., Ebinger, C., Lucazeau, F., and Al Lazki, A. 2011. The crustal structure of the northeastern Gulf of Aden continental margin: insights from wide-angle seismic data, Geophys. J. Int. 184, 575-594.

Watremez, L., Burov, E., d'Acremont, E., Leroy, S., Huet, B., Le Pourhiet, L., Bellahsen, N., 2013. Buoyancy and localizing properties of continental mantle lithosphere: Insights from thermomechanical models of the eastern Gulf of Aden. G3 14, 2800-2817.

Whitmarsh, R. B., Manatschal, G. and Minshull, T. A. 2001. Evolution of magma-poor continental margins from rifting to seafloor spreading. Nature, 413, 150–154, doi:10.1038/35093085.

Vinnik, L.P., 1977. Detection of waves converted from P to SV in the mantle. Phys. Earth Planet Inter., 15, 39-45.

Zandt, G., Myers, S. and Wallace, T., 1995. Crust and mantle structure across the Basin and Range-Colorado Plateau boundary at 37◦N latitude and implications for Cenozoic extensional mechanism. J. geophys. Res., 100, 10 529–10 548.

Zhu, L., 2000. Crustal structure across the San Andreas Fault, Southern California from teleseismic converted waves: Earth Planet. Sci. Lett., 179, 183-190.

Zhu, L. and Kanamori, H., 2000. Moho Depth Variation in Southern California from Teleseimic Receiver Function. J.Geophys. Res., 105, 2969-2980.

**Figures Captions**

**Figure 1. a)** and **b)** Landsat imagery and Sea-sat bathymetry showing the main tectonic features of the Gulf of Aden and surrounding areas. The large black arrows indicate the direction of plate motion in the region. The white lines show the location of the first magnetic anomaly (5d=17.6Ma) identified in the Gulf of Aden (d'Acremont et al 2006; Leroy et al. 2010a, 2012). **c)** Polar projection shows the distribution of seismic events, small circle interval is 30°. SSFZ: Shukra el Sheik Fracture Zone; AFFZ: Alula Fartak Fracture Zone; SHFZ: Socotra Hadbeen Fracture Zone; DSTF: Dead Sea Transform Fault, Owen TF: Owen Transform Fault.

**Figure 2.** Geological map of the study area showing geological units (modified from Leroy et al., 2012; Denele et al., 2012), location of YOCMAL temporary network of 24 seismic stations on Socotra and SOCY station, one of the Yemen-GFZ permanent seismic network.

**Figure 3.** Stacked receiver functions for the 24 seismic stations of the ANR-YOCMAL network and one permanent station on Socotra: a) for the eastern domain of Socotra, b-e) for the western domain of Socotra. The arrows represent the arrival of the Moho Pms (black), PpPs (red) and PpSs+PsPs (blue) phases from the Moho. See inset in f) for explanation of the Moho Pms and the multiple phase crustal paths.

**Table1.** Crustal thickness (H) and Vp/Vs ratio results for seismic stations on Socotra. The average crustal velocity used is 6.4 km/s. The average crustal velocity is based on previous studies of the velocity structure for the Arabian platform (e.g., Mooney et al., 1985; Al-Amri et al., 1998, 1999).

**Figure 4.** Individual receiver functions for 4 stations on Socotra. The receiver functions are organized by increasing backazimuth (red number right of the trace). The light vertical lines indicate arrival times for conversion phases (Pms and multiples) from the Moho for the maximum stacking amplitude.

**Figure 5.** Thickness (H) versus Vp/Vs ratio diagrams from the H-k stacking method for the 4 stations presented in Figure 4. The maximum stacking amplitude is indicated by the white point and corresponds to the value indicated in Table 1. The scale bar is the amplitude of stacking function.

**Figure 6.** Maps of crustal thicknesses (H) and Vp/Vs ratios calculated using the H-k method and average crustal velocity of 6.4 km/s. **a)** Geological map with the crustal thickness variations of Socotra and **b)** Geological map with the Vp/Vs ratio variations of Socotra.

**Figure 7.** Major tectonic features of Socotra and mapping of distinct zones based on average crustal thickness as listed in Table 1. Roman numbers corresponds to areas described in the text with a same average crustal thickness. Red lines: major tectonic features. MTZ: Momi Transfer zone; See the figure 1 caption for the type of stations.

**Figure 8.** Migrated cross-sections with the horizontal axis corresponding to the distance in km, centered at the mid-point of the profile. The Moho depth estimated from H-k stacking method is plotted with the small triangles. Red color indicates velocity increase with depth, and blue color, velocity decrease with depth. Scale bar shows amplitude of positive (red) and negative (blue) polarities of arrivals. The interpretation of each cross-section is presented in the right panel, HTZ: Hadibo Transfer Zone MTZ: Momi Transfer Zone, **a)** SW-NE cross section at westernmost Socotra (inset for location of the cross-section A-B) **b)** SW-NE cross section in the middle of the western Socotra (inset for location of the cross-section C-D), **c)** E-W cross section along the island parallel to the southern coast (inset for location of the cross-section E-F) and **d)** E-W cross section along the island parallel to the northern coast (inset for location G-H).

**Figure 9. a -** Seismic velocity models for DIAA station (eastern Socotra) obtained from the NA method (Sambridge, 1999a) and waveform matches between the observed stacked receiver functions (red) and the predicted ones (green) based on the best models (red lines in the left diagrams) . The grey area indicates the range of models employed by the algorithm. The best 1000 models are indicated in green, the red line corresponds to the best fit both for S-wave velocity and Vp/Vs ratio and the white line is the average velocity model. **b –** the same models for SOCY station (western Socotra)

**Figure 10.** Regional map showing Moho depths based on the results of this study at Socotra island and previous RF studies in Dhofar-Oman the northern conjugate margin (Tiberi et al., 2007; Al-Hashmi et al., 2011), active seismic, gravity and magnetic studies offshore to the west of Socotra (d'Acremont et al., 2006), active seismic offshore Oman - northeastern Gulf of Aden (Leroy et al., 2010a). The roman numbers at the western end of Socotra island indicates the areas with a uniform average crustal thickness as described in the result section. The blue line corresponds to the first magnetic anomaly identified (5d; 17.6 Ma;

Leroy et al., 2010a). SHFZ: Socotra Hadbeen Fracture zone; Alula Fartak Fracture zone; MFZ: Momi Fracture zone; HTZ: Hadibo Fracture Zone

**Figure 11.** Schematic transect of a magma-poor margin showing the distinct crustal domains (modified from Leroy et al., 2010a; Mohn et al., 2012) compared to distinct area of Socotra island based on crustal thickness variations. ZE: Zone of Exhumation.

highlights

- Continental margin segmentation with two distinct domains forming Socotra island
- Outcropping of a necking zone in a magma-poor continental margin setting
- Pre-existing transfer zone dipping westward which may extend to the lower crust

| Station name | Number of RF | Latitude (N) | Longitude (E) | Elevation (m) | Crustal thickness (H, km) | Vp/Vs Ratio | Error in depth (km) | Error In Vp/Vs |
|---|---|---|---|---|---|---|---|---|
| ADAH | 44 | 12.6513 | 53.6509 | 217 | 21.6 | 1.77 | 0.83 | 0.033 |
| AMAD | 27 | 12.5072 | 53.5747 | 134 | 23.2 | 1.84 | 0.43 | 0.029 |
| BIRZ | 20 | 12.4786 | 53.9209 | 882 | 30.2 | 1.73 | 1.1 | 0.027 |
| DANA | 35 | 12.3907 | 53.5230 | 251 | 26.6 | 1.80 | 0.66 | 0.038 |
| DESH | 29 | 12.5830 | 54.2392 | 89 | 23.6 | 1.77 | 1.08 | 0.034 |
| DIAA | 41 | 12.6509 | 53.5299 | 76 | 19.6 | 1.65 | 0.39 | 0.016 |
| EERS | 18 | 12.4269 | 53.7719 | 151 | 28.2 | 1.73 | 2.11 | 0.055 |
| GSFO | 56 | 12.4774 | 54.1399 | 134 | 27.6 | 1.78 | 0.74 | 0.026 |
| HAME | 32 | 12.5166 | 53.6305 | 124 | 20.2 | 1.76 | 0.47 | 0.023 |
| HEIL | 28 | 12.6266 | 54.1296 | 87 | 28.6 | 1.70 | 0.99 | 0.032 |
| KABH | 36 | 12.4059 | 53.7080 | 137 | 26.8 | 1.76 | 0.33 | 0.017 |
| KADA | 45 | 12.6993 | 53.6449 | 35 | 16.8 | 1.89 | 0.59 | 0.037 |
| LISK | 23 | 12.5840 | 53.7185 | 44 | 22.0 | 1.77 | 0.48 | 0.045 |
| MALA | 38 | 12.6550 | 53.4380 | 680 | 21.4 | 1.71 | 0.61 | 0.052 |
| MDAP | 23 | 12.5382 | 53.7054 | 52 | 23.4 | 1.77 | 0.52 | 0.031 |
| RIGI | 38 | 12.5304 | 53.5067 | 239 | 23.0 | 1.77 | 1.07 | 0.043 |
| RUSU | 25 | 12.6605 | 53.5755 | 100 | 16.4 | 1.71 | 1.69 | 0.054 |
| SAFN | 34 | 12.5261 | 53.4649 | 156 | 23.4 | 1.73 | 0.63 | 0.048 |
| SAYH | 34 | 12.5340 | 54.3903 | 360 | 22.4 | 1.82 | 0.6 | 0.044 |
| SHER | 20 | 12.5356 | 53.3777 | 41 | 22.2 | 1.70 | 1.04 | 0.046 |
| SHRQ | 26 | 12.6196 | 53.7583 | 16 | 20.0 | 1.80 | 1.17 | 0.058 |
| SHUA | 39 | 12.5932 | 53.4957 | 691 | 21.2 | 1.83 | 0.32 | 0.021 |
| SOCY | 30 | 12.5195 | 53.9874 | 804 | 28.4 | 1.78 | 0.213 | 0.012 |
| TROB | 55 | 12.5630 | 53.9327 | 150 | 28.2 | 1.94 | 1.39 | 0.043 |
| WURE | 56 | 12.4176 | 53.5806 | 179 | 26.4 | 1.73 | 0.39 | 0.032 |

Table1

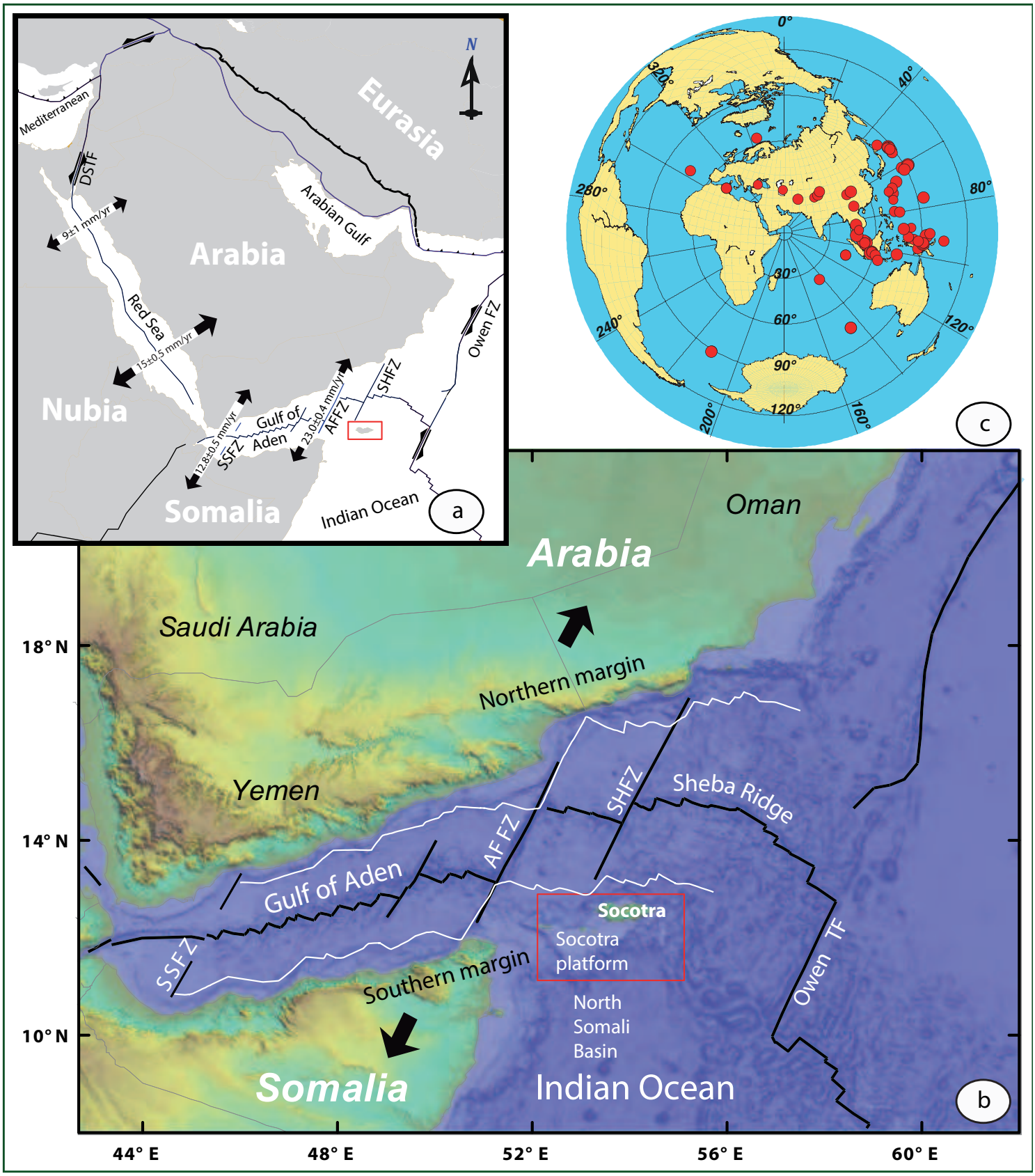
N
Eurasia
Mediterranean
DSTF
9±1 mm/yr
Arabian Gulf
Arabia
Red Sea
15±0.5 mm/yr
Owen FZ
SHFZ
Nubia
Gulf of Aden
AFFZ
23.0±0.4 mm/yr
12.8±0.5 mm/yr
SSFZ
Somalia
Indian Ocean
a
0°
40°
80°
120°
160°
200°
240°
280°
320°
30°
60°
90°
120°
c
Oman
Arabia
Saudi Arabia
Northern margin
Yemen
SHFZ
Sheba Ridge
AF FZ
Gulf of Aden
Socotra
Socotra platform
SSFZ
Southern margin
Owen TF
North Somali Basin
Somalia
Indian Ocean
b
18° N
14° N
10° N
44° E
48° E
52° E
56° E
60° E

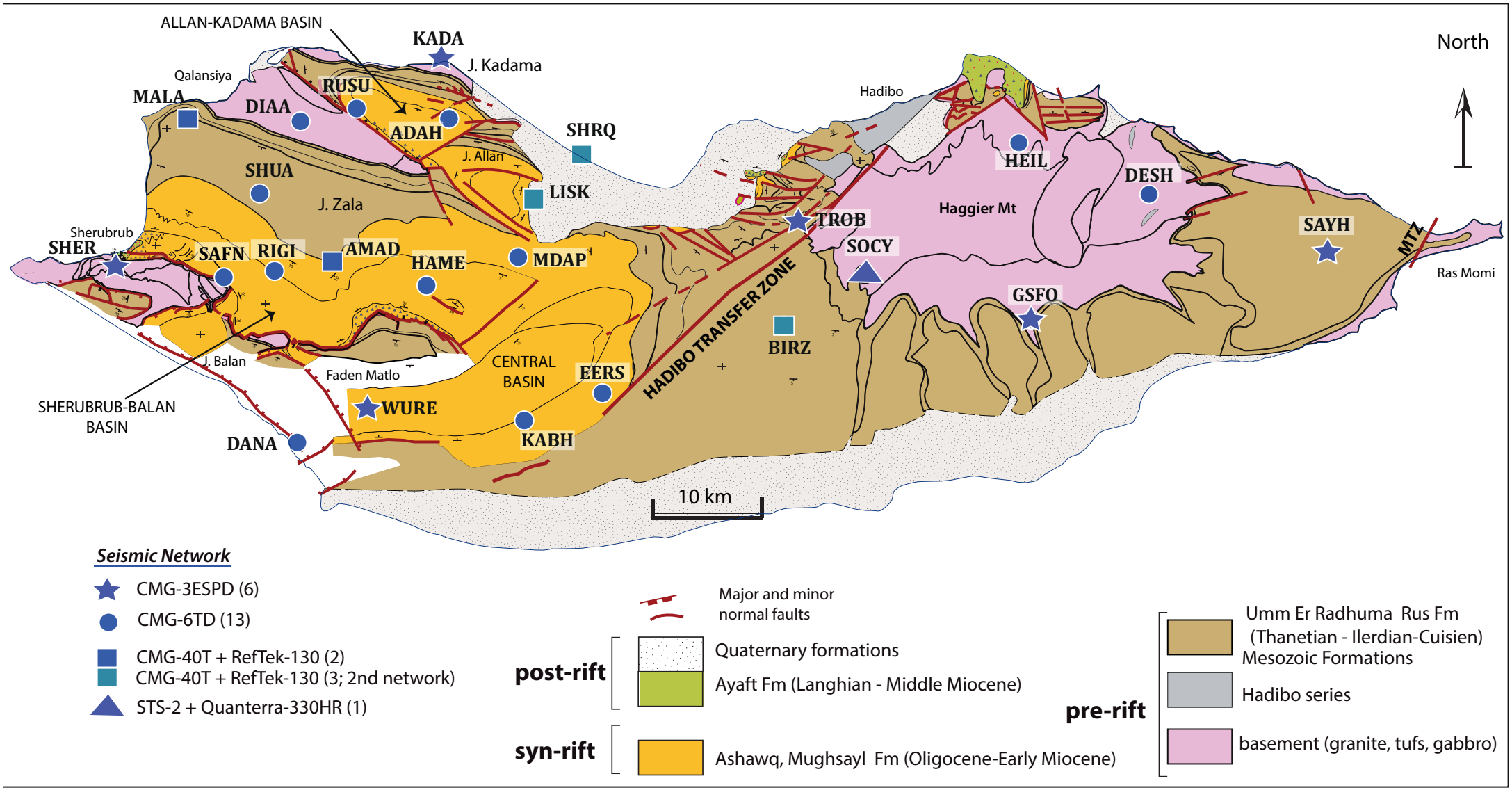
ALLAN-KADAMA BASIN
KADA
J. Kadama
North
Qalansiya
MALA
DIAA
RUSU
ADAH
SHRQ
Hadibo
HEIL
DESH
J. Allan
SHUA
J. Zala
LISK
Haggier Mt
TROB
SOCY
SAYH
MTZ
Ras Momi
Sherubrub
SHER
SAFN
RIGI
AMAD
HAME
MDAP
GSFO
HADIBO TRANSFER ZONE
BIRZ
J. Balan
Faden Matlo
CENTRAL
BASIN
EERS
WURE
KABH
SHERUBRUB-BALAN
BASIN
DANA
10 km
Seismic Network
CMG-3ESPD (6)
CMG-6TD (13)
CMG-40T + RefTek-130 (2)
CMG-40T + RefTek-130 (3; 2nd network)
STS-2 + Quanterra-330HR (1)
Major and minor
normal faults
post-rift
Quaternary formations
Ayaft Fm (Langhian - Middle Miocene)
syn-rift
Ashawq, Mughsayl Fm (Oligocene-Early Miocene)
pre-rift
Umm Er Radhuma Rus Fm
(Thanetian - Ilerdian-Cuisien)
Mesozoic Formations
Hadibo series
basement (granite, tufs, gabbro)

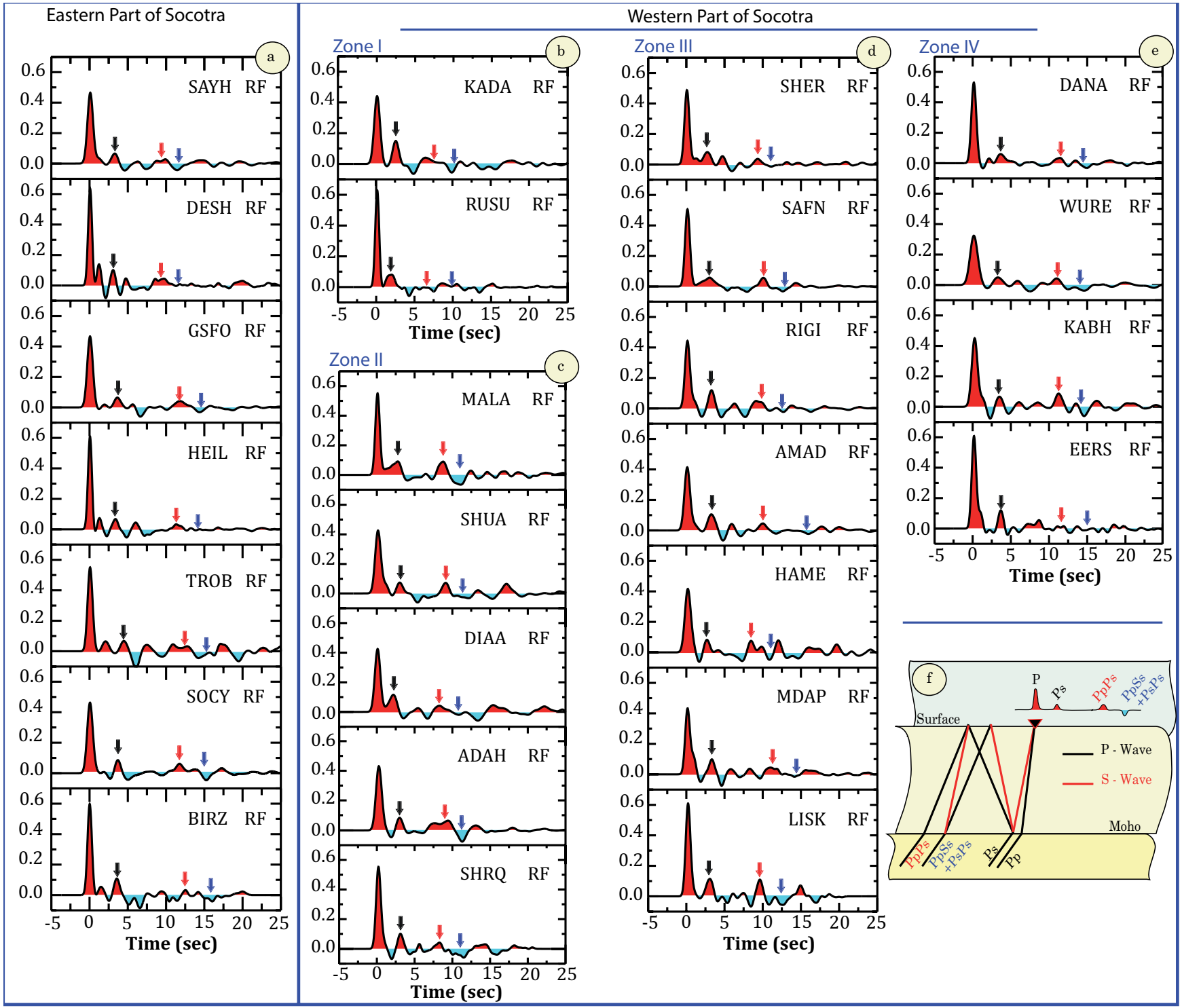
Eastern Part of Socotra
Western Part of Socotra
Zone I
Zone II
Zone III
Zone IV
a
b
c
d
e
f
SAYH RF
DESH RF
GSFO RF
HEIL RF
TROB RF
SOCY RF
BIRZ RF
KADA RF
RUSU RF
MALA RF
SHUA RF
DIAA RF
ADAH RF
SHRQ RF
SHER RF
SAFN RF
RIGI RF
AMAD RF
HAME RF
MDAP RF
LISK RF
DANA RF
WURE RF
KABH RF
EERS RF
Time (sec)
P
Ps
PpPs
PpSs +PsPs
Surface
P - Wave
S - Wave
Moho
Pp

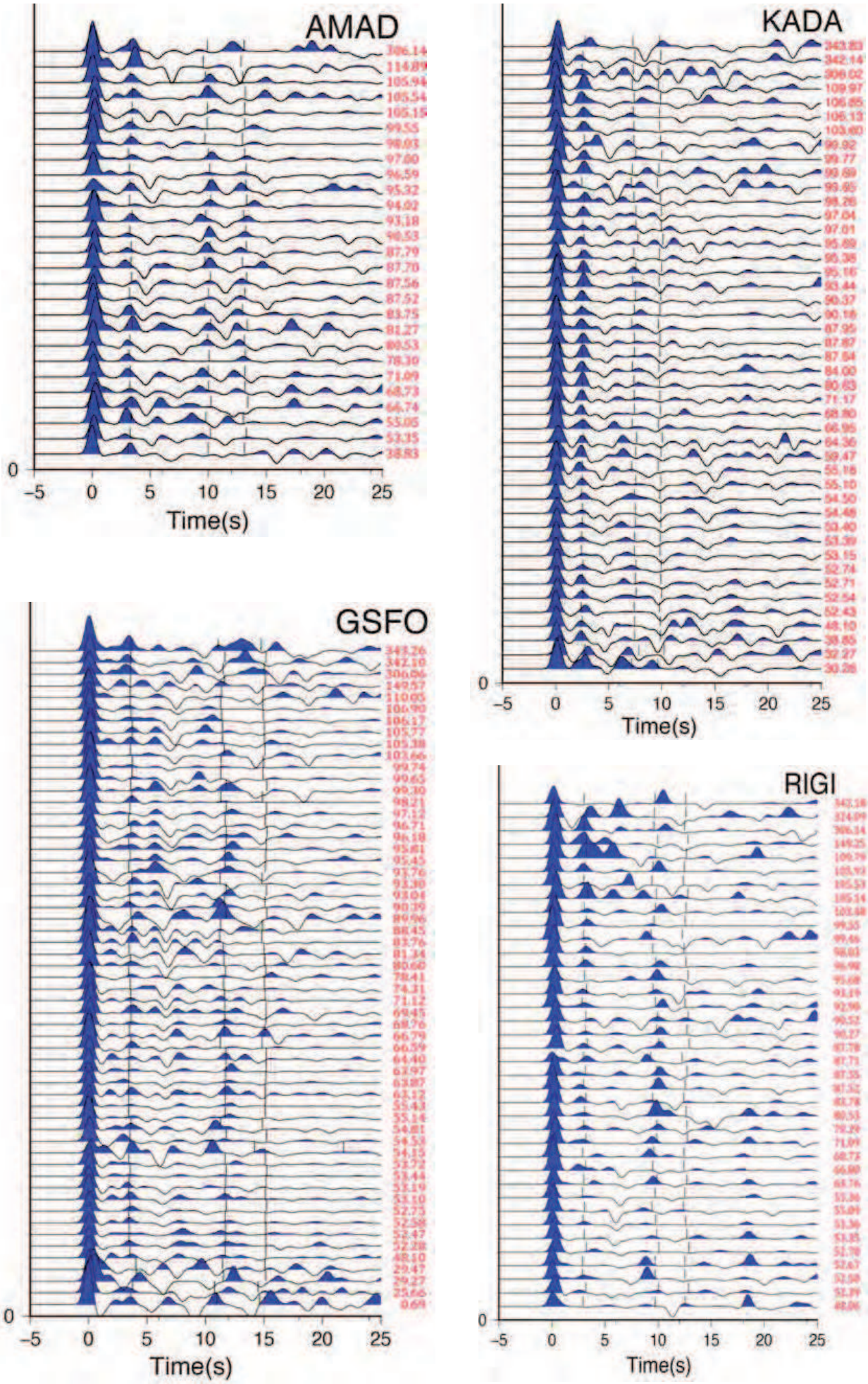


Fig4 Ahmed et al

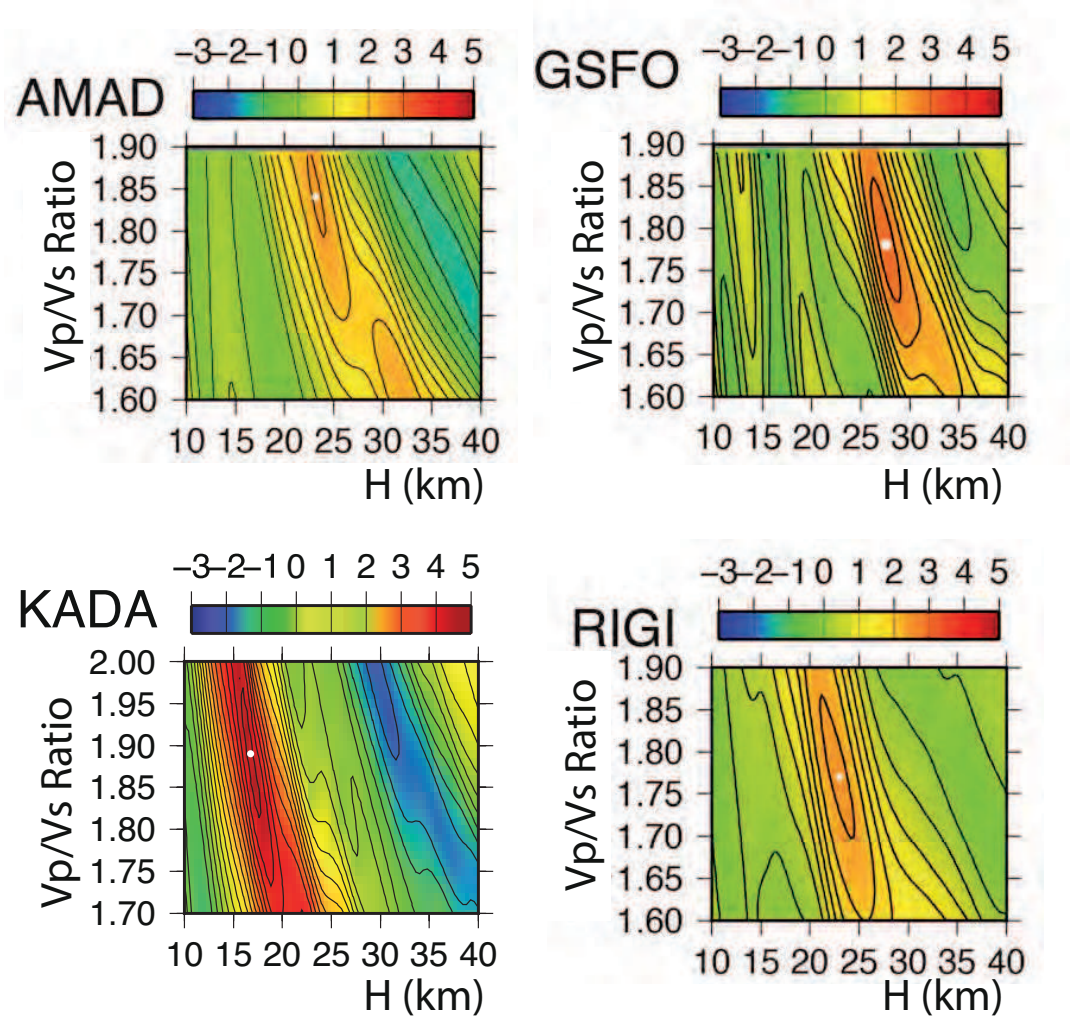


Fig5 Ahmed et al

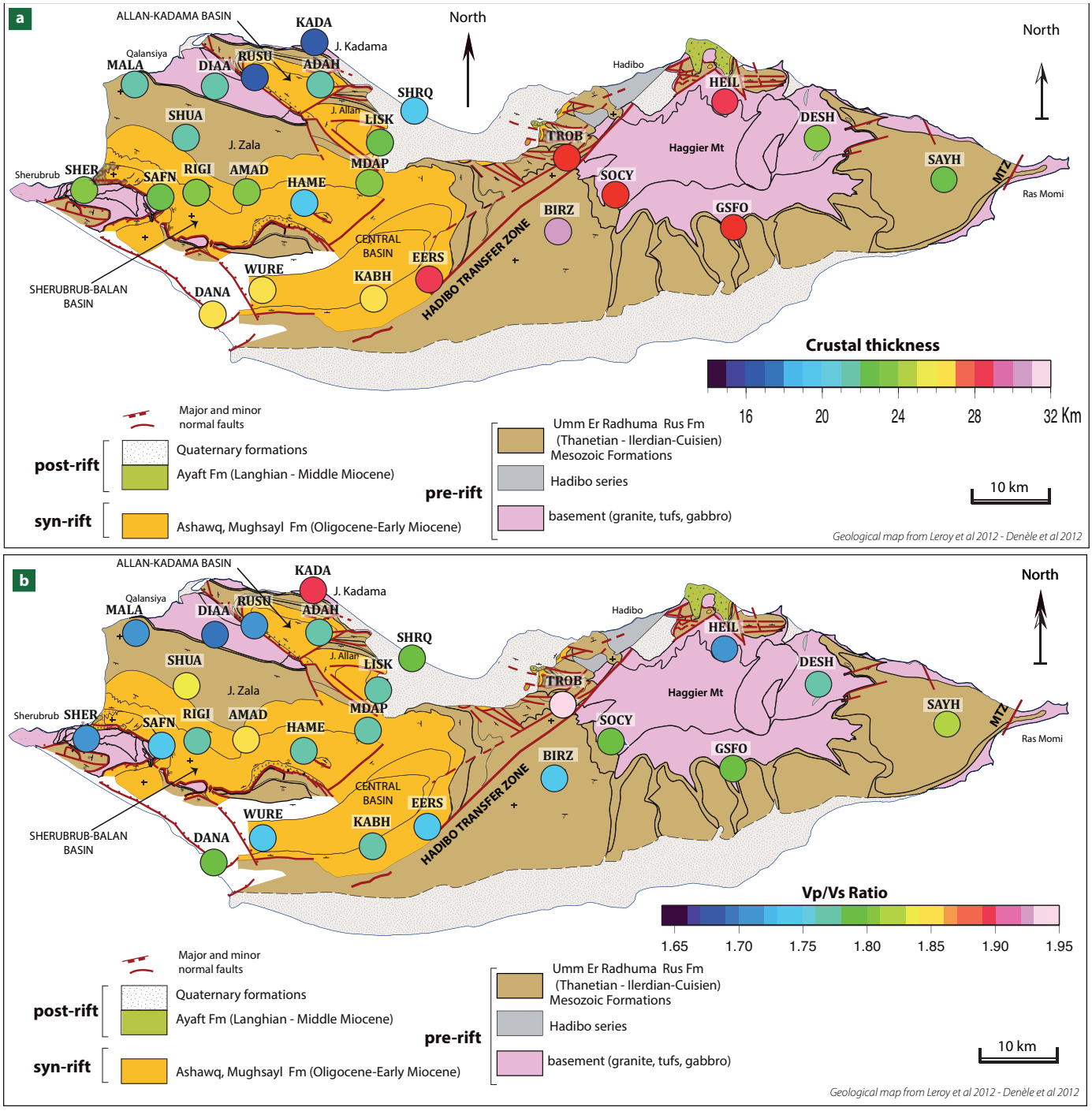
a
ALLAN-KADAMA BASIN
KADA
J. Kadama
North
Qalansiya
MALA
DIAA
RUSU
ADAH
SHRQ
Hadibo
HEIL
SHUA
J. Allan
LISK
DESH
J. Zala
TROB
Haggier Mt
Sherubrub
SHER
SAFN
RIGI
AMAD
MDAP
SAYH
HAME
SOCY
MTZ
Ras Momi
BIRZ
GSFO
CENTRAL BASIN
EERS
WURE
KABH
HADIBO TRANSFER ZONE
SHERUBRUB-BALAN BASIN
DANA
Crustal thickness
16
20
24
28
32 Km
Major and minor normal faults
Quaternary formations
post-rift
Ayaft Fm (Langhian - Middle Miocene)
syn-rift
Ashawq, Mughsayl Fm (Oligocene-Early Miocene)
pre-rift
Umm Er Radhuma Rus Fm (Thanetian - Ilerdian-Cuisien)
Mesozoic Formations
Hadibo series
basement (granite, tufs, gabbro)
10 km
Geological map from Leroy et al 2012 - Denèle et al 2012
b
ALLAN-KADAMA BASIN
KADA
J. Kadama
North
Qalansiya
MALA
DIAA
RUSU
ADAH
SHRQ
Hadibo
HEIL
SHUA
J. Allan
LISK
DESH
J. Zala
TROB
Haggier Mt
Sherubrub
SHER
SAFN
RIGI
AMAD
MDAP
SAYH
HAME
SOCY
MTZ
Ras Momi
BIRZ
GSFO
CENTRAL BASIN
EERS
WURE
KABH
HADIBO TRANSFER ZONE
SHERUBRUB-BALAN BASIN
DANA
Vp/Vs Ratio
1.65
1.70
1.75
1.80
1.85
1.90
1.95
Major and minor normal faults
Quaternary formations
post-rift
Ayaft Fm (Langhian - Middle Miocene)
syn-rift
Ashawq, Mughsayl Fm (Oligocene-Early Miocene)
pre-rift
Umm Er Radhuma Rus Fm (Thanetian - Ilerdian-Cuisien)
Mesozoic Formations
Hadibo series
basement (granite, tufs, gabbro)
10 km
Geological map from Leroy et al 2012 - Denèle et al 2012

Fig 6

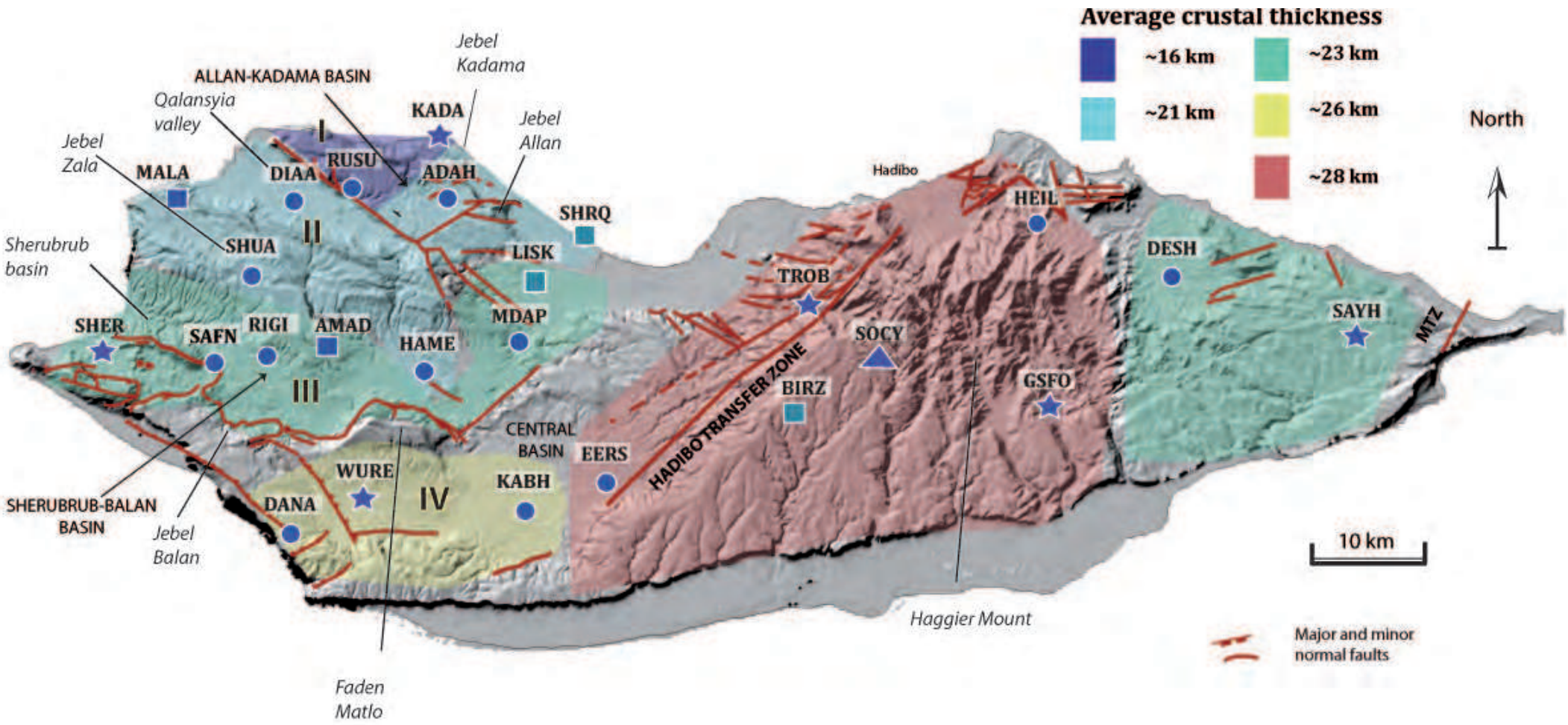
Average crustal thickness
~16 km
~21 km
~23 km
~26 km
~28 km
North
10 km
Major and minor normal faults
ALLAN-KADAMA BASIN
Jebel Kadama
Qalansyia valley
Jebel Zala
Jebel Allan
Sherubrub basin
SHERUBRUB-BALAN BASIN
Jebel Balan
Faden Matlo
Haggier Mount
Hadibo
HADIBO TRANSFER ZONE
CENTRAL BASIN
MTZ
I
II
III
IV
KADA
RUSU
DIAA
ADAH
MALA
SHUA
SHRQ
LISK
MDAP
SHER
SAFN
RIGI
AMAD
HAME
WURE
DANA
KABH
EERS
TROB
SOCY
BIRZ
HEIL
GSFO
DESH
SAYH

Fig 7

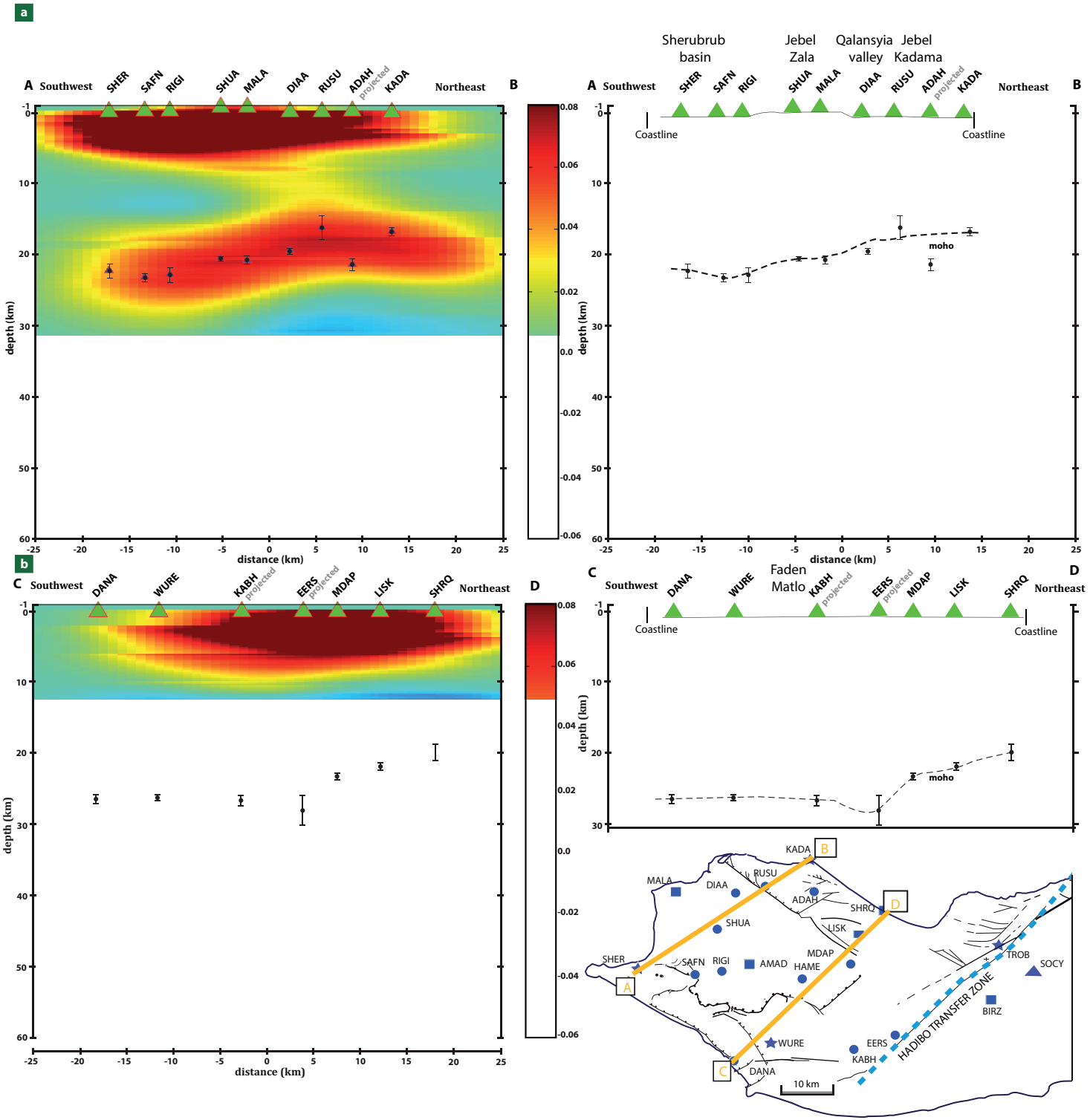
a
A Southwest
SHER
SAFN
RIGI
SHUA
MALA
DIAA
RUSU
ADAH projected
KADA
Northeast B
depth (km)
distance (km)
Sherubrub basin
Jebel Zala
Qalansyia valley
Jebel Kadama
Coastline
moho
b
C Southwest
DANA
WURE
KABH projected
EERS projected
MDAP
LISK
SHRQ
Northeast D
Faden Matlo
HADIBO TRANSFER ZONE
TROB
SOCY
BIRZ
AMAD
HAME
10 km

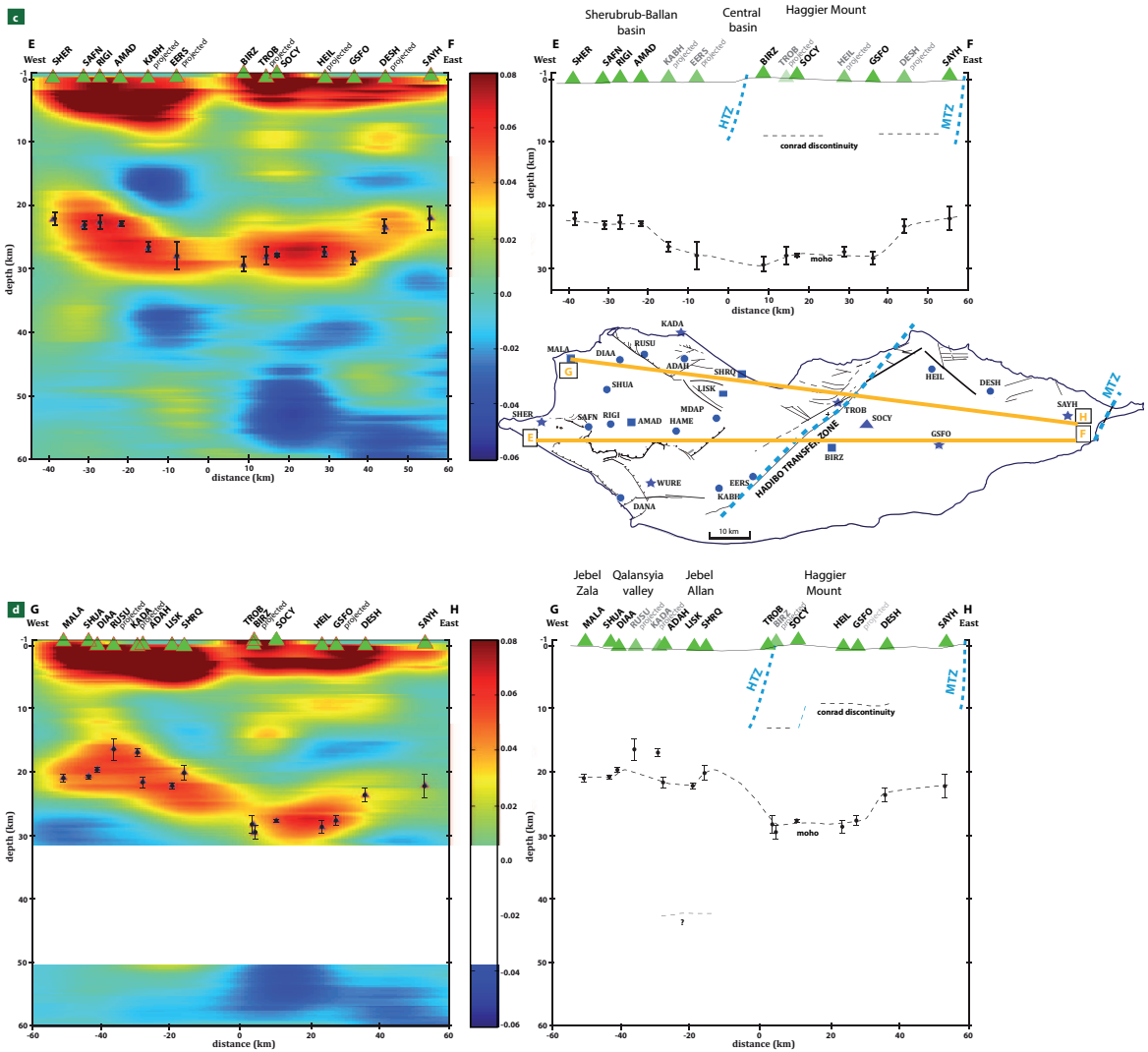
c
d
West
East
depth (km)
distance (km)
Sherubrub-Ballan basin
Central basin
Haggier Mount
Jebel Zala
Qalansyia valley
Jebel Allan
conrad discontinuity
moho
HTZ
MTZ
HADIBO TRANSFER ZONE
10 km

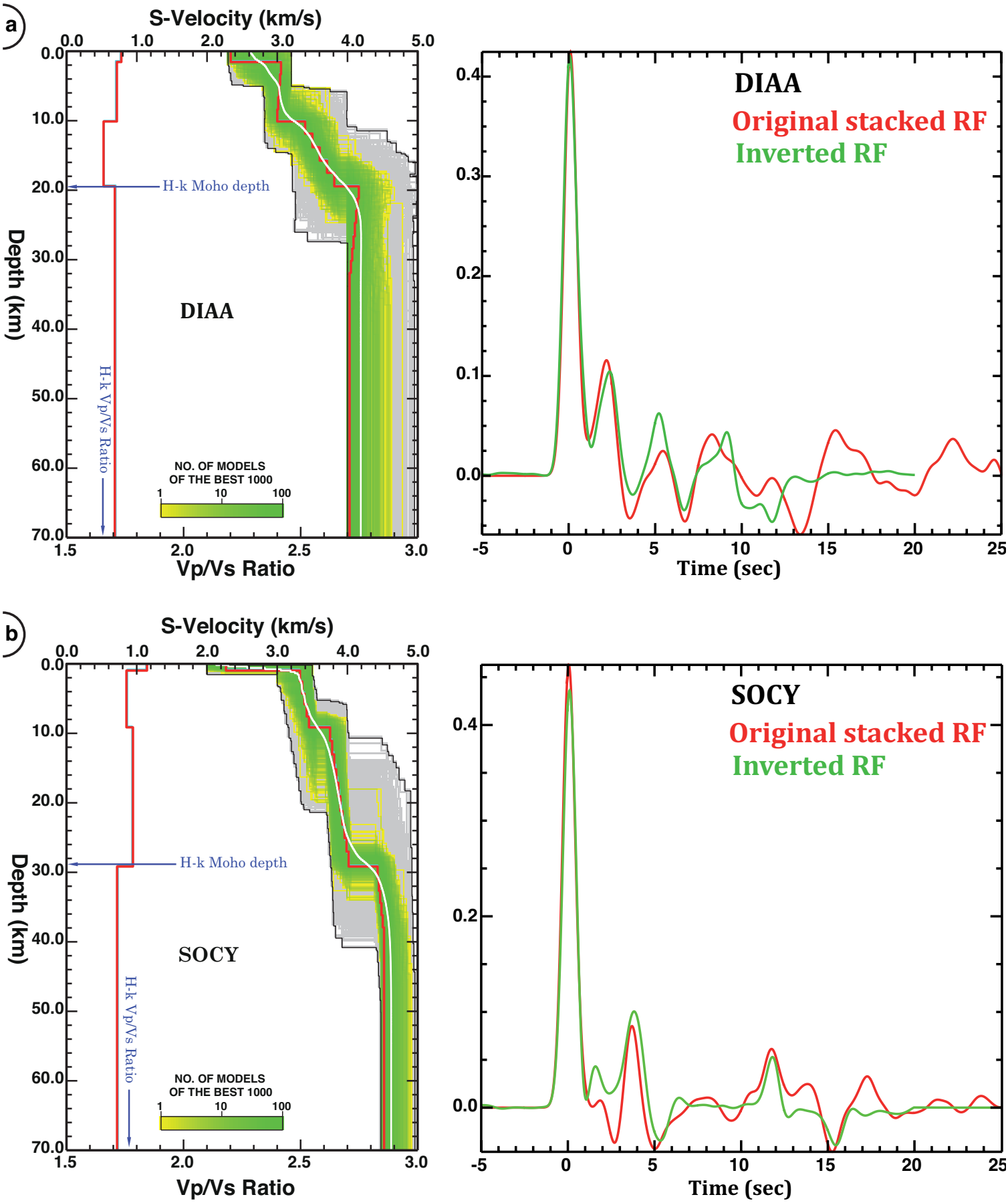
a
S-Velocity (km/s)
0.0
1.0
2.0
3.0
4.0
5.0
Depth (km)
H-k Moho depth
DIAA
H-k Vp/Vs Ratio
NO. OF MODELS
OF THE BEST 1000
1
10
100
Vp/Vs Ratio
DIAA
Original stacked RF
Inverted RF
Time (sec)
b
SOCY

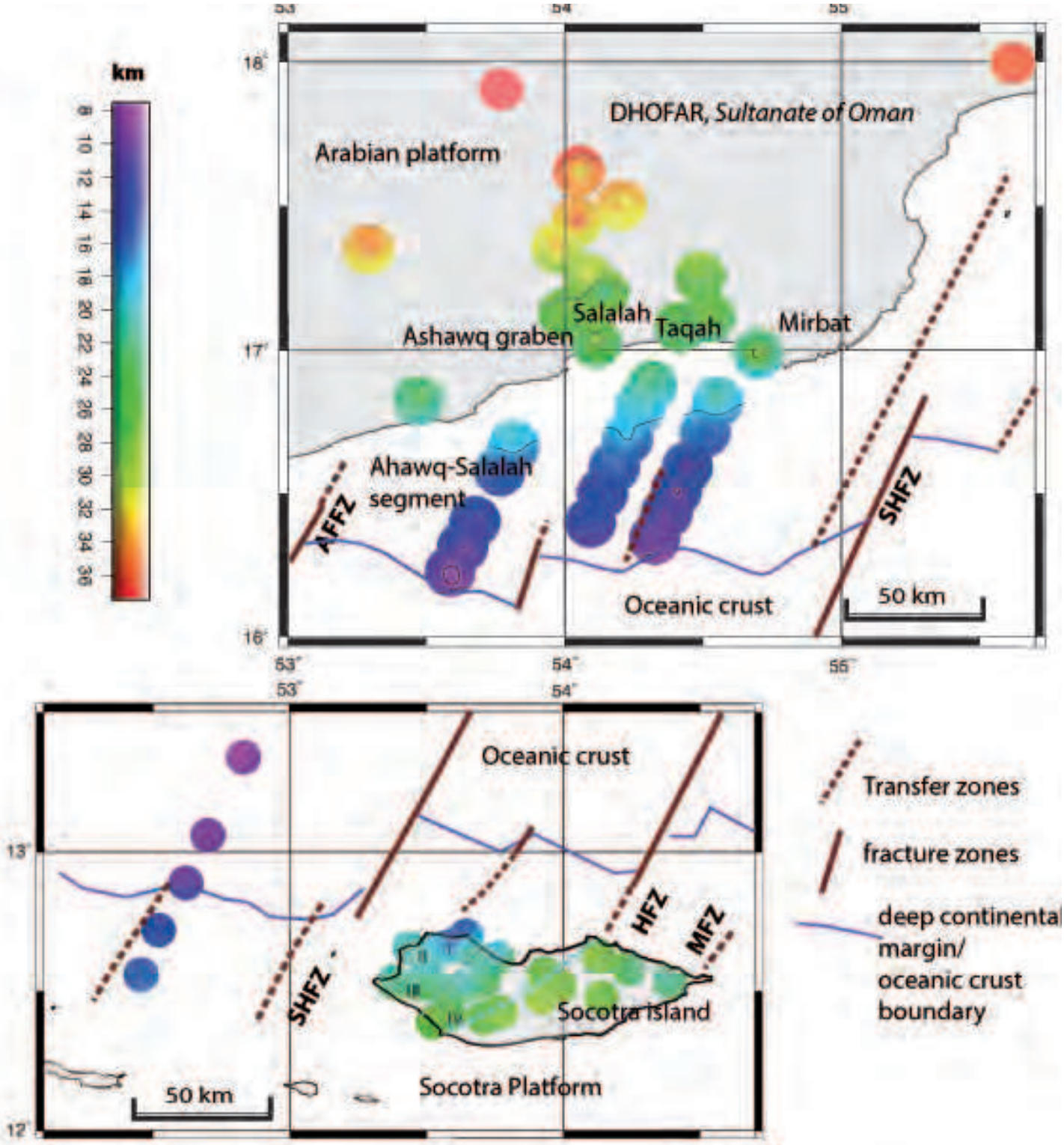
km
8 10 12 14 16 18 20 22 24 26 28 30 32 34 36
DHOFAR, Sultanate of Oman
Arabian platform
Salalah
Taqah
Mirbat
Ashawq graben
Ahawq-Salalah segment
AFFZ
SHFZ
Oceanic crust
50 km
Oceanic crust
SHFZ
HFZ
MFZ
Socotra Island
Socotra Platform
50 km
Transfer zones
fracture zones
deep continental margin/ oceanic crust boundary

fig10

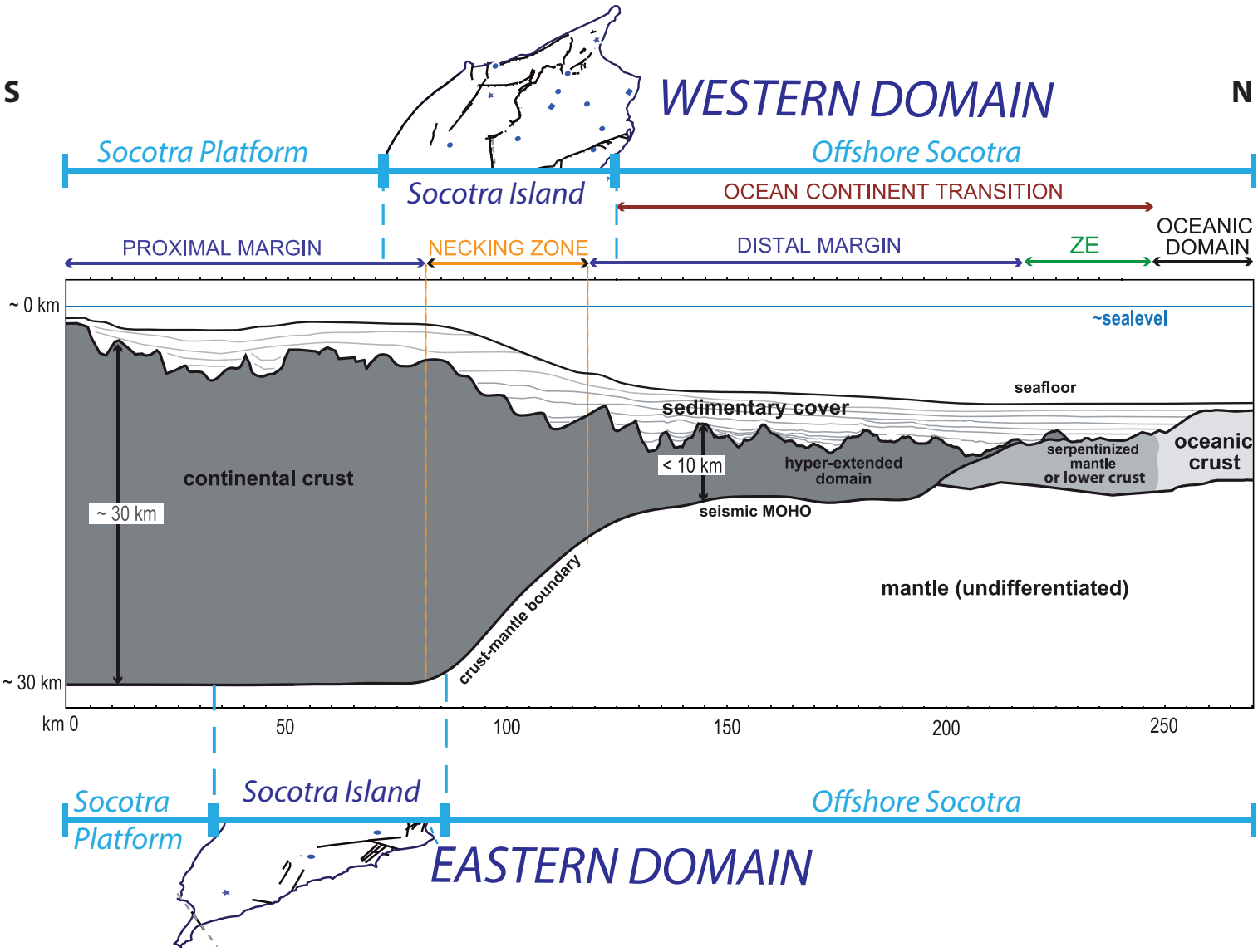
S
N
WESTERN DOMAIN
Socotra Platform
Offshore Socotra
Socotra Island
OCEAN CONTINENT TRANSITION
PROXIMAL MARGIN
NECKING ZONE
DISTAL MARGIN
ZE
OCEANIC DOMAIN
~ 0 km
~sealevel
seafloor
sedimentary cover
continental crust
< 10 km
hyper-extended domain
serpentinized mantle or lower crust
oceanic crust
~ 30 km
seismic MOHO
crust-mantle boundary
mantle (undifferentiated)
~ 30 km
km 0
50
100
150
200
250
Socotra Platform
Socotra Island
Offshore Socotra
EASTERN DOMAIN

**Supplementary materials: Ahmed et al. Socotra**

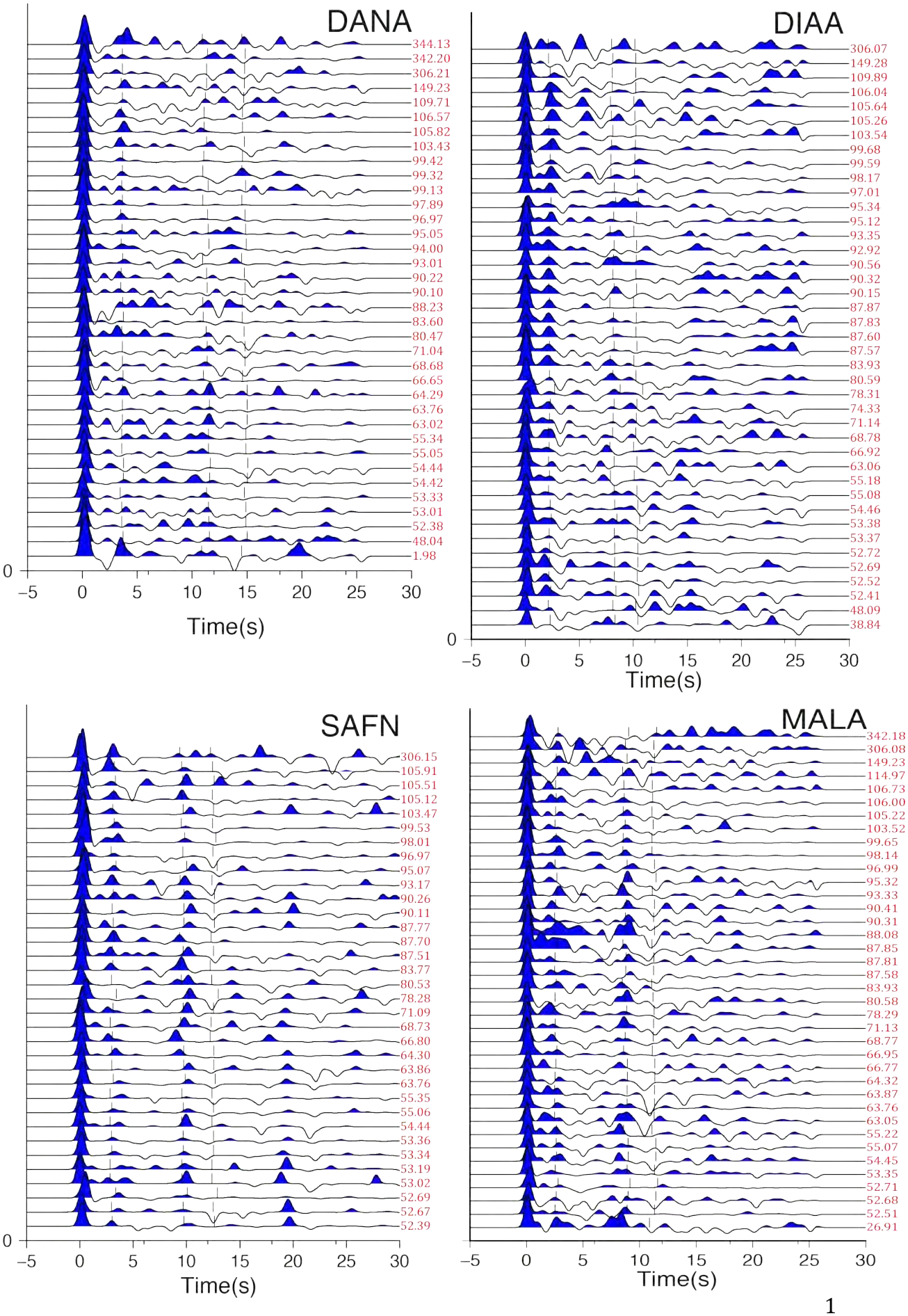

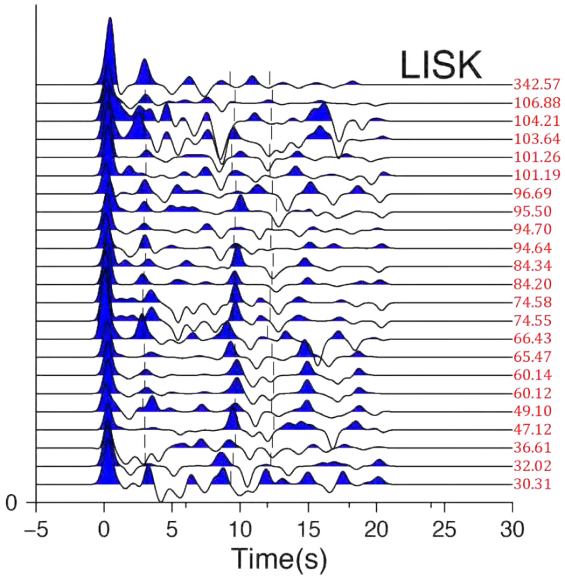
LISK
342.57
106.88
104.21
103.64
101.26
101.19
96.69
95.50
94.70
94.64
84.34
84.20
74.58
74.55
66.43
65.47
60.14
60.12
49.10
47.12
36.61
32.02
30.31
0
–5 0 5 10 15 20 25 30
Time(s)

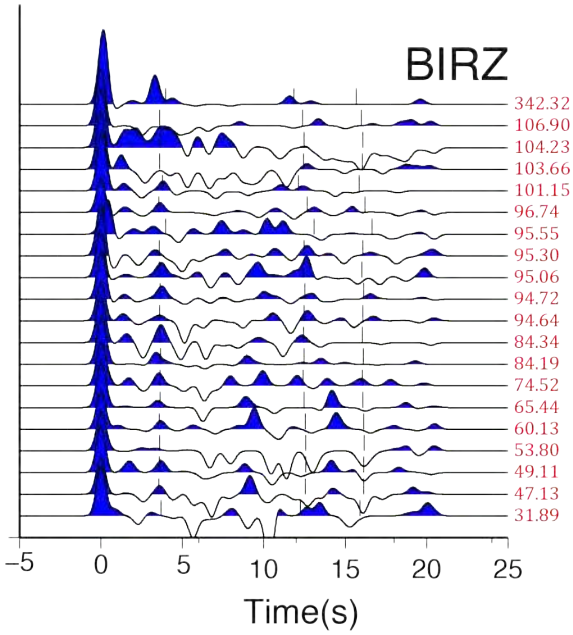
BIRZ
342.32
106.90
104.23
103.66
101.15
96.74
95.55
95.30
95.06
94.72
94.64
84.34
84.19
74.52
65.44
60.13
53.80
49.11
47.13
31.89
–5 0 5 10 15 20 25
Time(s)

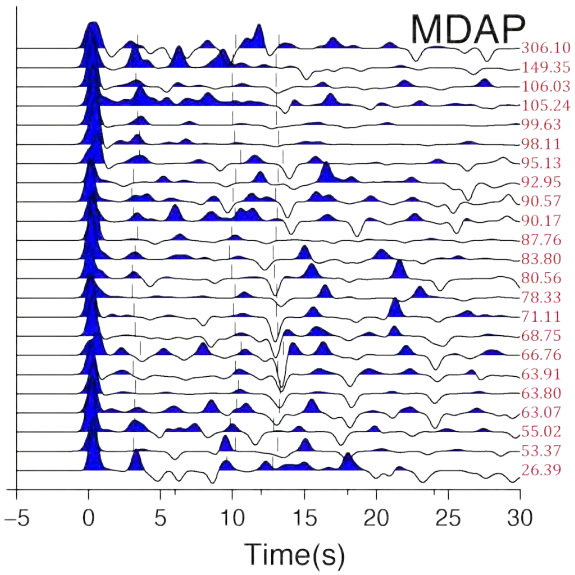
MDAP
306.10
149.35
106.03
105.24
99.63
98.11
95.13
92.95
90.57
90.17
87.76
83.80
80.56
78.33
71.11
68.75
66.76
63.91
63.80
63.07
55.02
53.37
26.39
–5 0 5 10 15 20 25 30
Time(s)

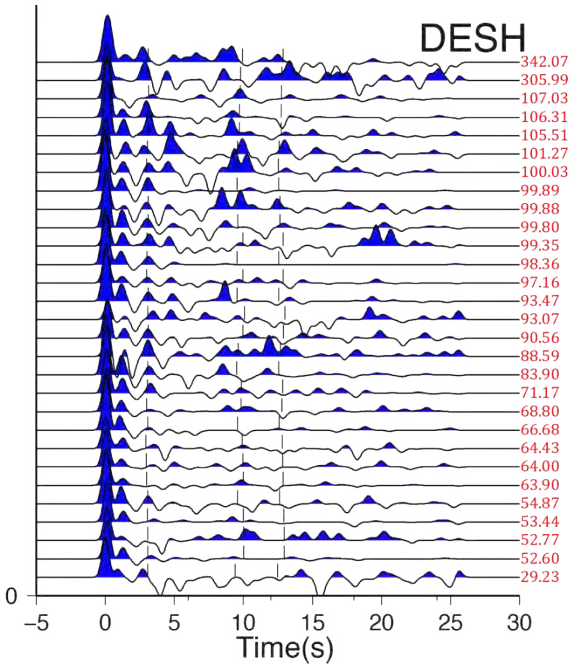
DESH
342.07
305.99
107.03
106.31
105.51
101.27
100.03
99.89
99.88
99.80
99.35
98.36
97.16
93.47
93.07
90.56
88.59
83.90
71.17
68.80
66.68
64.43
64.00
63.90
54.87
53.44
52.77
52.60
29.23
0
–5 0 5 10 15 20 25 30
Time(s)

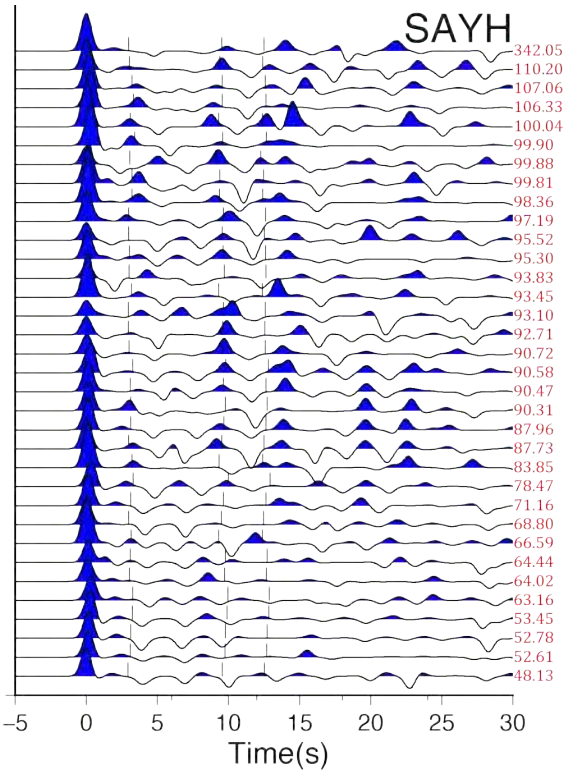
SAYH
342.05
110.20
107.06
106.33
100.04
99.90
99.88
99.81
98.36
97.19
95.52
95.30
93.83
93.45
93.10
92.71
90.72
90.58
90.47
90.31
87.96
87.73
83.85
78.47
71.16
68.80
66.59
64.44
64.02
63.16
53.45
52.78
52.61
48.13
–5 0 5 10 15 20 25 30
Time(s)

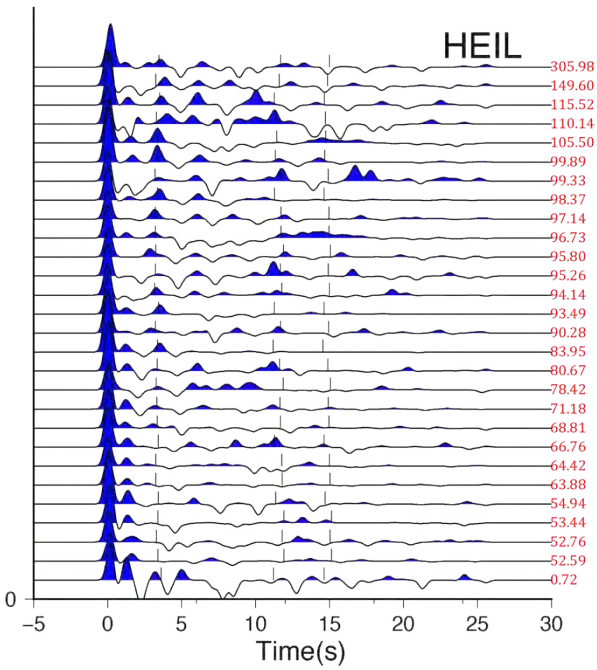
HEIL
305.98
149.60
115.52
110.14
105.50
99.89
99.33
98.37
97.14
96.73
95.80
95.26
94.14
93.49
90.28
83.95
80.67
78.42
71.18
68.81
66.76
64.42
63.88
54.94
53.44
52.76
52.59
0.72
0
–5 0 5 10 15 20 25 30
Time(s)

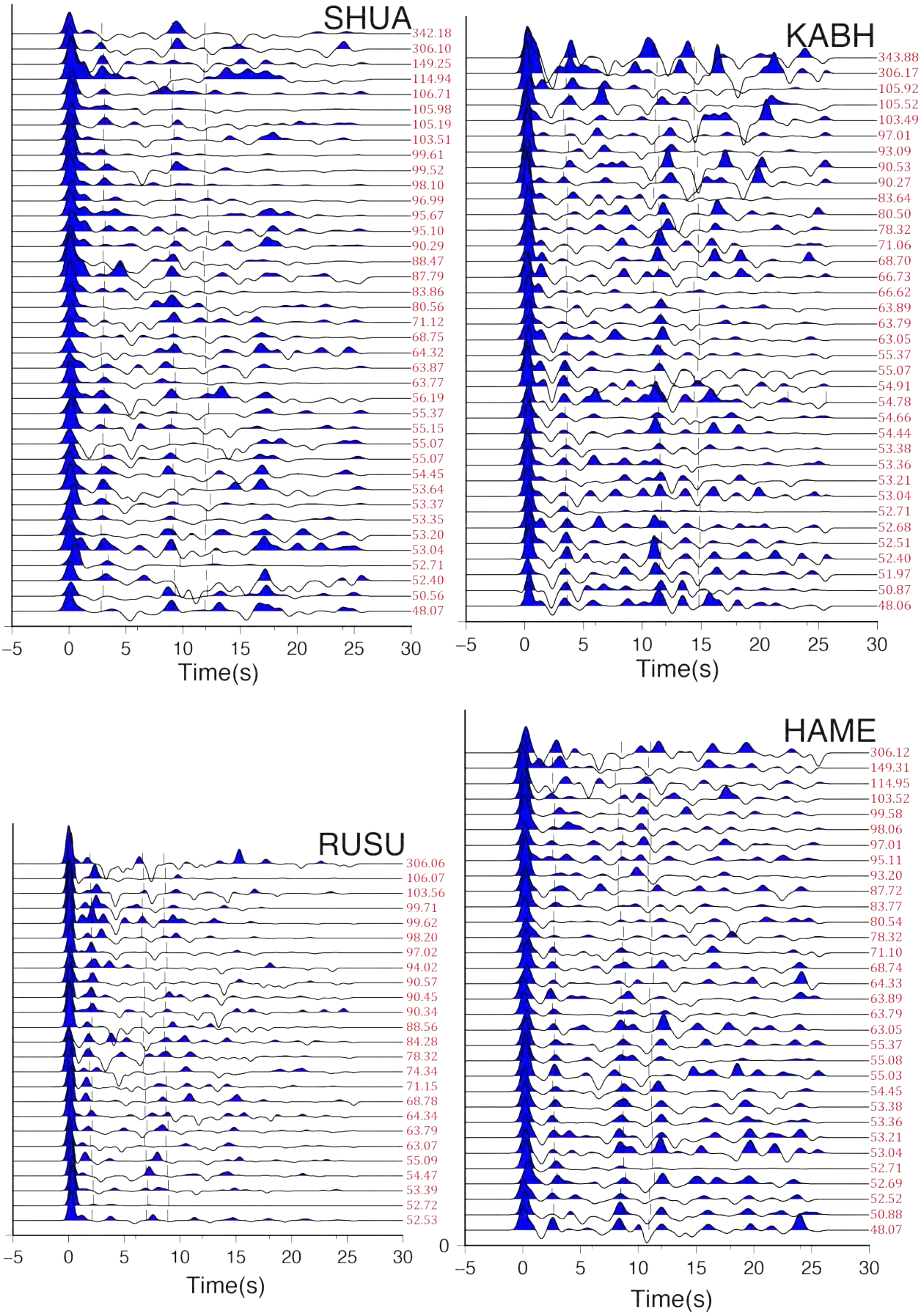
SHUA
342.18
306.10
149.25
114.94
106.71
105.98
105.19
103.51
99.61
99.52
98.10
96.99
95.67
95.10
90.29
88.47
87.79
83.86
80.56
71.12
68.75
64.32
63.87
63.77
56.19
55.37
55.15
55.07
55.07
54.45
53.64
53.37
53.35
53.20
53.04
52.71
52.40
50.56
48.07
–5 0 5 10 15 20 25 30
Time(s)
KABH
343.88
306.17
105.92
105.52
103.49
97.01
93.09
90.53
90.27
83.64
80.50
78.32
71.06
68.70
66.73
66.62
63.89
63.79
63.05
55.37
55.07
54.91
54.78
54.66
54.44
53.38
53.36
53.21
53.04
52.71
52.68
52.51
52.40
51.97
50.87
48.06
–5 0 5 10 15 20 25 30
Time(s)
RUSU
306.06
106.07
103.56
99.71
99.62
98.20
97.02
94.02
90.57
90.45
90.34
88.56
84.28
78.32
74.34
71.15
68.78
64.34
63.79
63.07
55.09
54.47
53.39
52.72
52.53
–5 0 5 10 15 20 25 30
Time(s)
HAME
306.12
149.31
114.95
103.52
99.58
98.06
97.01
95.11
93.20
87.72
83.77
80.54
78.32
71.10
68.74
64.33
63.89
63.79
63.05
55.37
55.08
55.03
54.45
53.38
53.36
53.21
53.04
52.71
52.69
52.52
50.88
48.07
0
–5 0 5 10 15 20 25 30
Time(s)

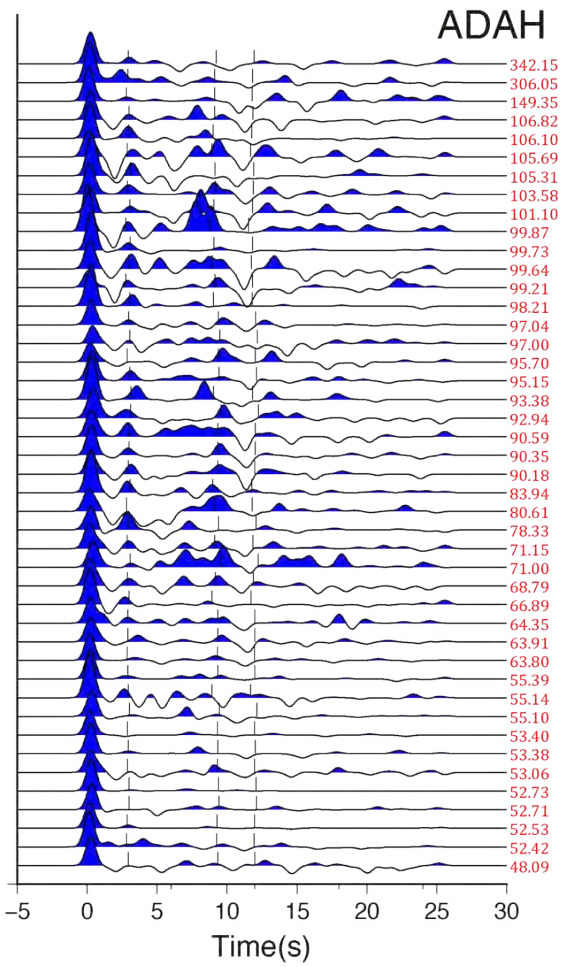
ADAH
342.15
306.05
149.35
106.82
106.10
105.69
105.31
103.58
101.10
99.87
99.73
99.64
99.21
98.21
97.04
97.00
95.70
95.15
93.38
92.94
90.59
90.35
90.18
83.94
80.61
78.33
71.15
71.00
68.79
66.89
64.35
63.91
63.80
55.39
55.14
55.10
53.40
53.38
53.06
52.73
52.71
52.53
52.42
48.09
–5 0 5 10 15 20 25 30
Time(s)

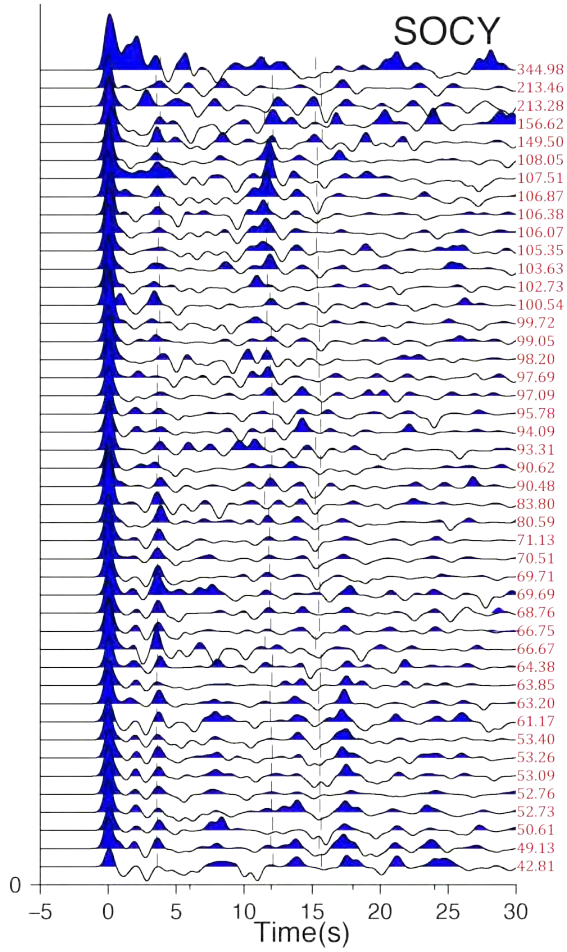
SOCY
344.98
213.46
213.28
156.62
149.50
108.05
107.51
106.87
106.38
106.07
105.35
103.63
102.73
100.54
99.72
99.05
98.20
97.69
97.09
95.78
94.09
93.31
90.62
90.48
83.80
80.59
71.13
70.51
69.71
69.69
68.76
66.75
66.67
64.38
63.85
63.20
61.17
53.40
53.26
53.09
52.76
52.73
50.61
49.13
42.81
0
–5 0 5 10 15 20 25 30
Time(s)

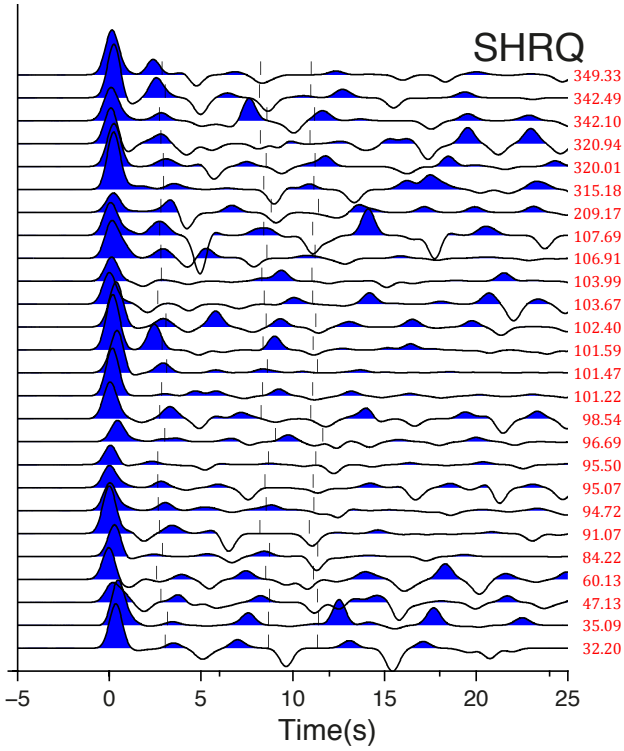
SHRQ
349.33
342.49
342.10
320.94
320.01
315.18
209.17
107.69
106.91
103.99
103.67
102.40
101.59
101.47
101.22
98.54
96.69
95.50
95.07
94.72
91.07
84.22
60.13
47.13
35.09
32.20
–5 0 5 10 15 20 25
Time(s)

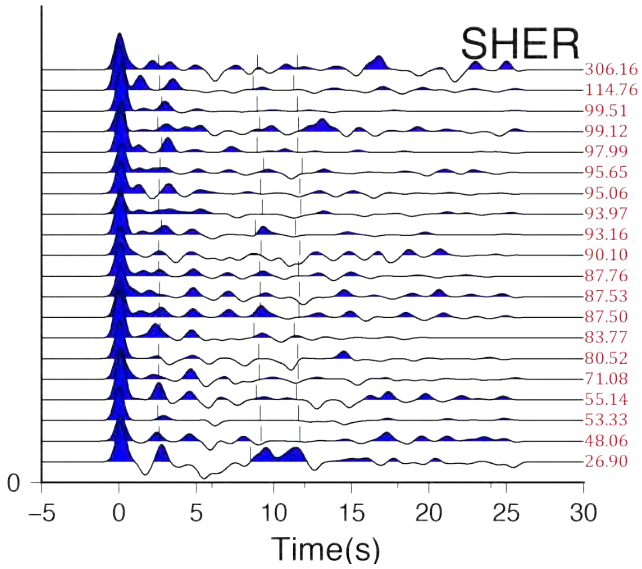
SHER
306.16
114.76
99.51
99.12
97.99
95.65
95.06
93.97
93.16
90.10
87.76
87.53
87.50
83.77
80.52
71.08
55.14
53.33
48.06
26.90
0
–5 0 5 10 15 20 25 30
Time(s)

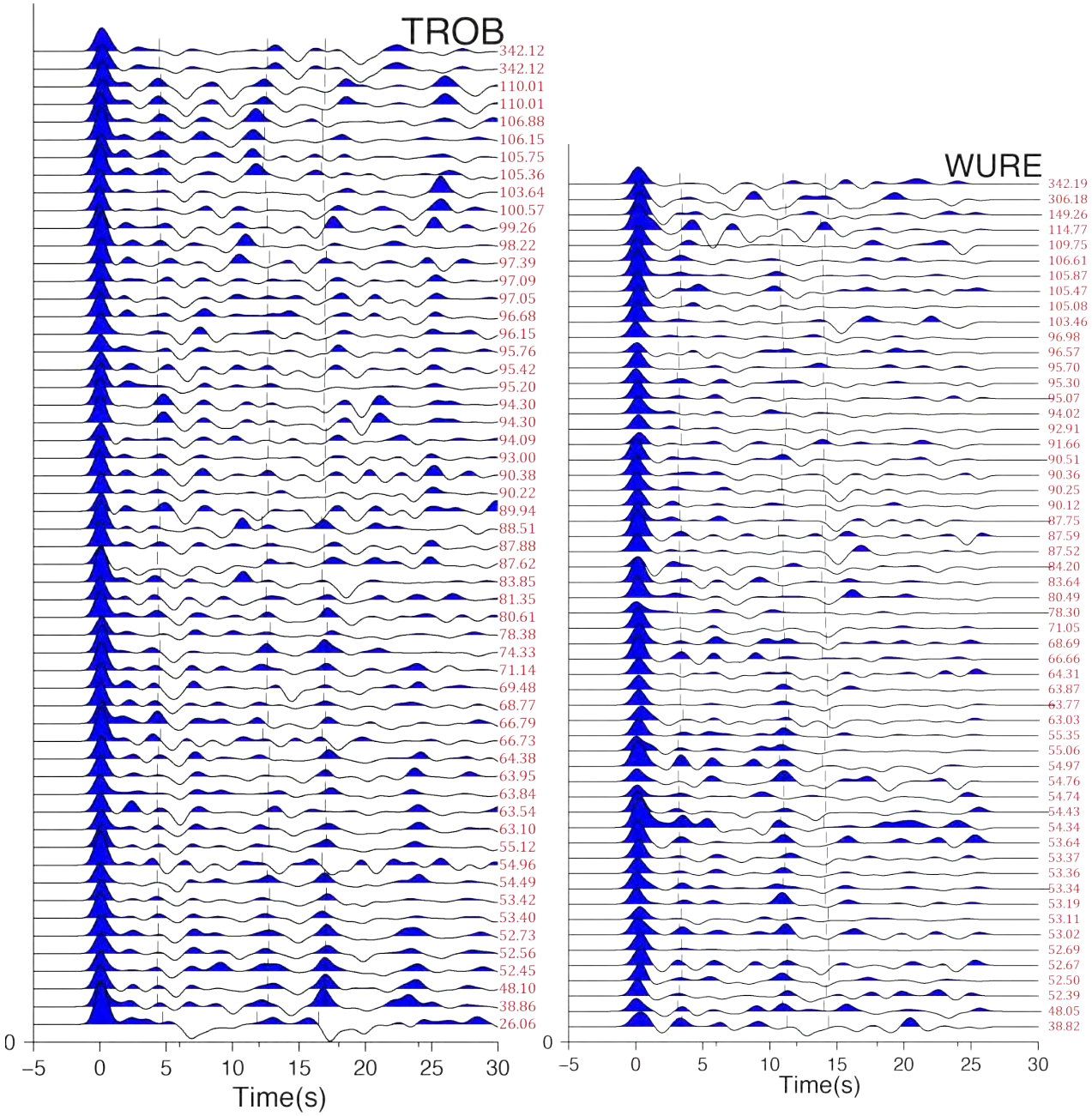


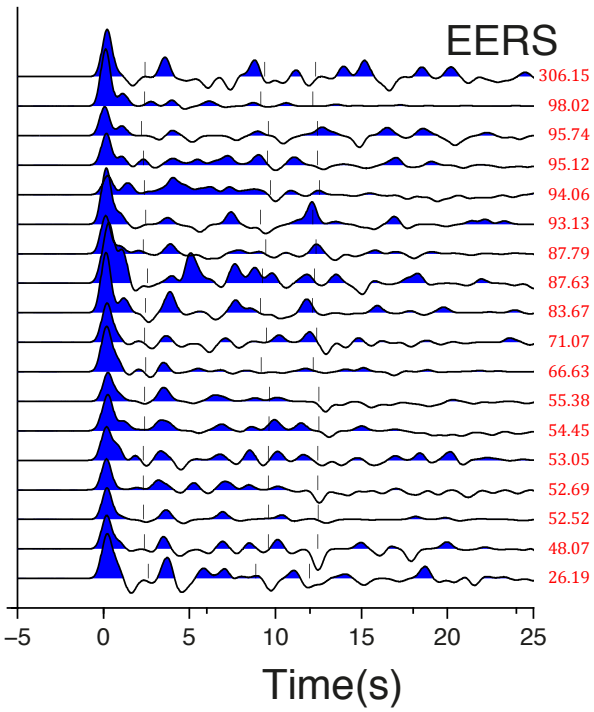


**Figure S1:**

Receiver functions for 21 stations of the Socotra island study. The receiver functions are organized by increasing backazimuth (red number right of the trace). The light vertical lines indicate arrival times for conversion phases (Pms and multiples) from the Moho for the maximum stacking amplitude.

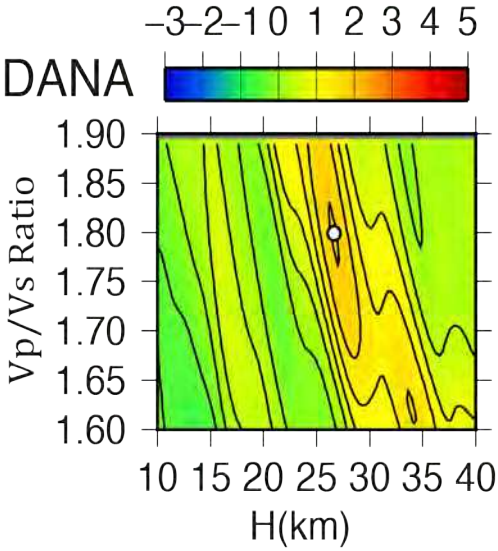
DANA
–3 –2 –1 0 1 2 3 4 5
Vp/Vs Ratio
1.90
1.85
1.80
1.75
1.70
1.65
1.60
10 15 20 25 30 35 40
H(km)

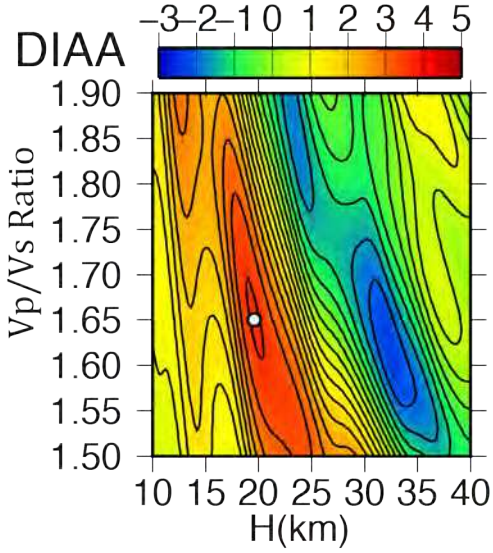
DIAA
–3 –2 –1 0 1 2 3 4 5
Vp/Vs Ratio
1.90
1.85
1.80
1.75
1.70
1.65
1.60
1.55
1.50
10 15 20 25 30 35 40
H(km)

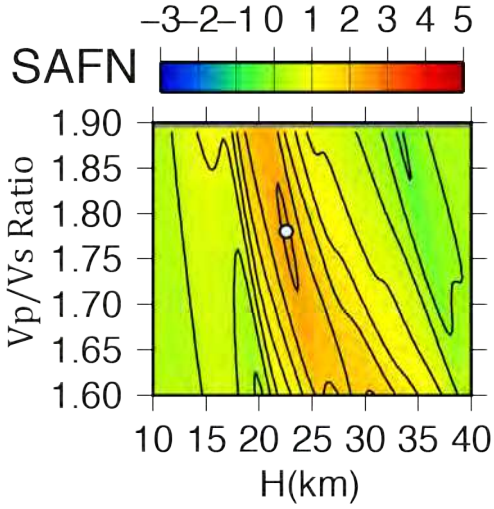
SAFN
–3 –2 –1 0 1 2 3 4 5
Vp/Vs Ratio
1.90
1.85
1.80
1.75
1.70
1.65
1.60
10 15 20 25 30 35 40
H(km)

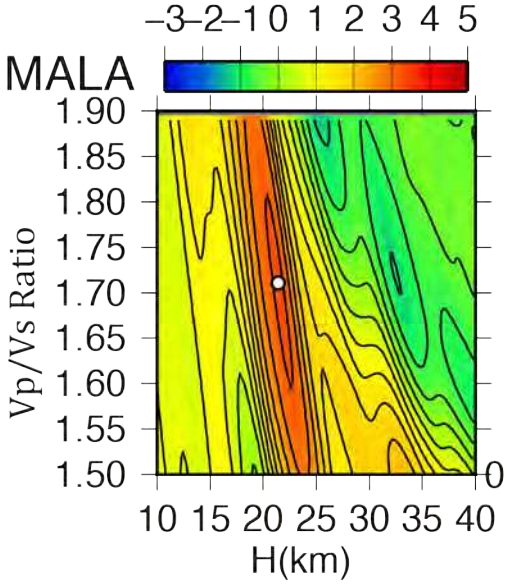
MALA
–3 –2 –1 0 1 2 3 4 5
Vp/Vs Ratio
1.90
1.85
1.80
1.75
1.70
1.65
1.60
1.55
1.50
0
10 15 20 25 30 35 40
H(km)

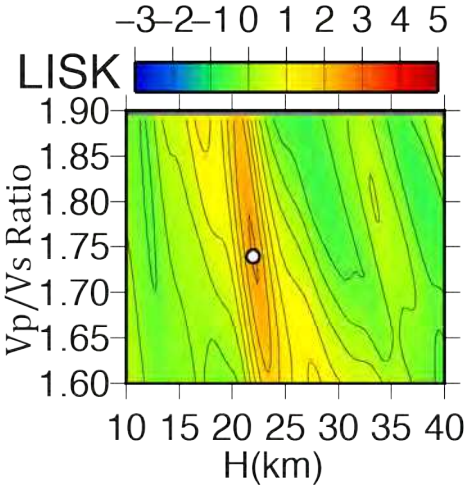
LISK
–3 –2 –1 0 1 2 3 4 5
Vp/Vs Ratio
1.90
1.85
1.80
1.75
1.70
1.65
1.60
10 15 20 25 30 35 40
H(km)

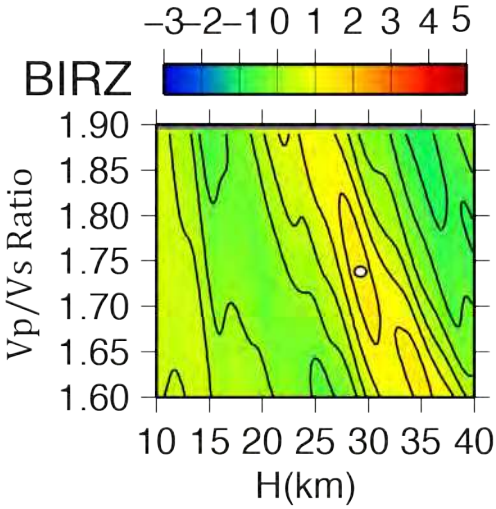
BIRZ
–3 –2 –1 0 1 2 3 4 5
Vp/Vs Ratio
1.90
1.85
1.80
1.75
1.70
1.65
1.60
10 15 20 25 30 35 40
H(km)

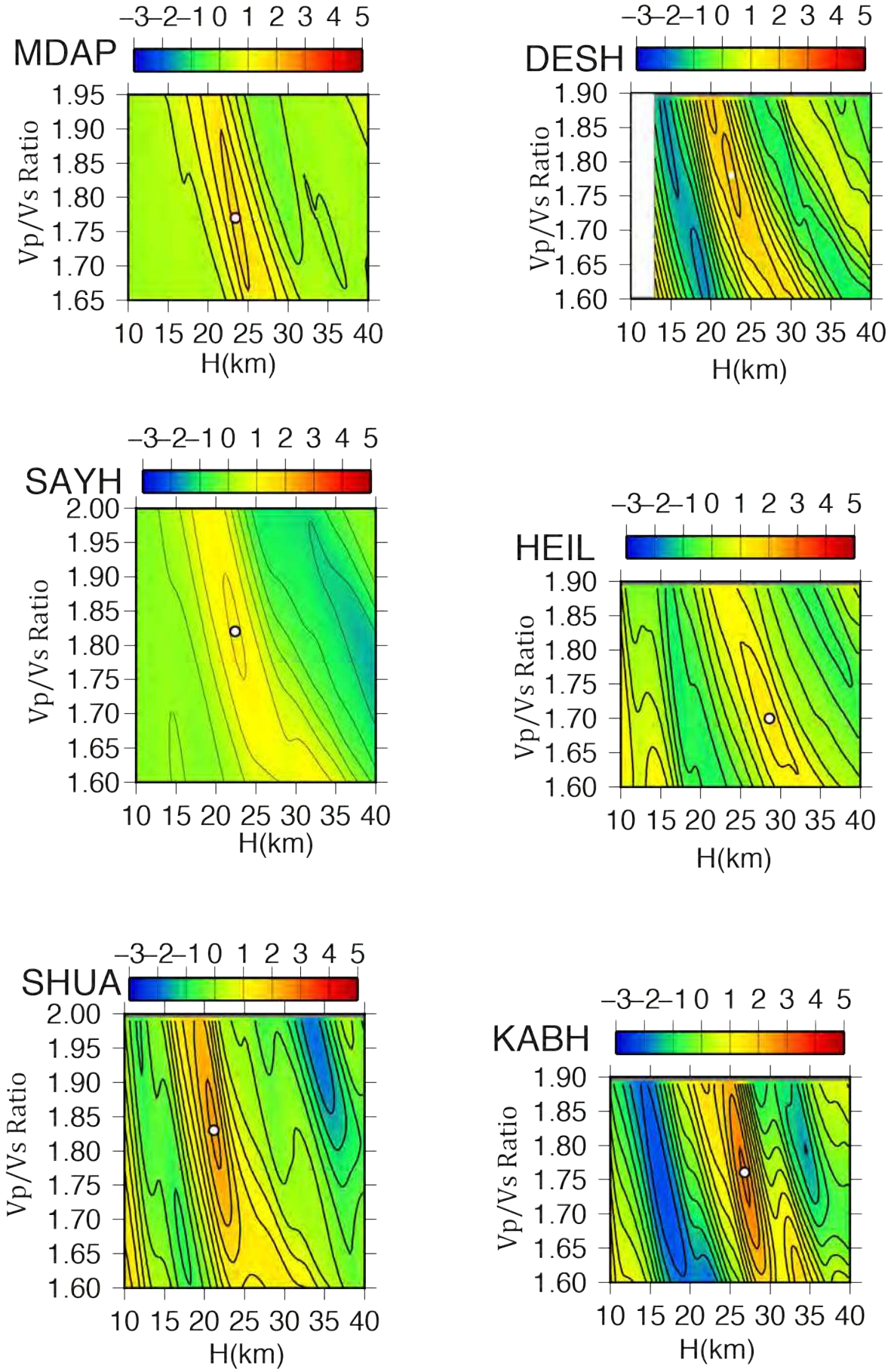
MDAP
DESH
SAYH
HEIL
SHUA
KABH
–3 –2 –1 0 1 2 3 4 5
Vp/Vs Ratio
H(km)
10 15 20 25 30 35 40
1.60 1.65 1.70 1.75 1.80 1.85 1.90 1.95 2.00

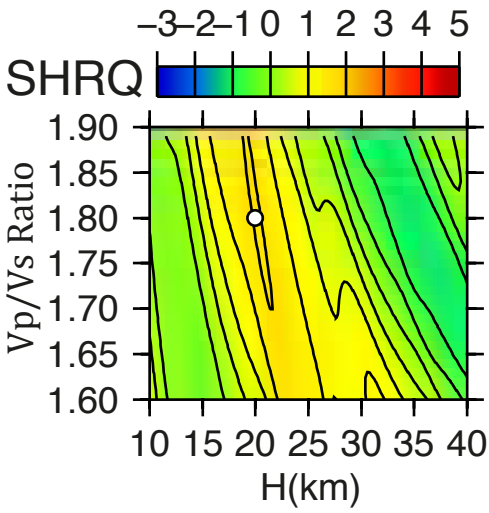
SHRQ
–3 –2 –1 0 1 2 3 4 5
Vp/Vs Ratio
1.90
1.85
1.80
1.75
1.70
1.65
1.60
10 15 20 25 30 35 40
H(km)

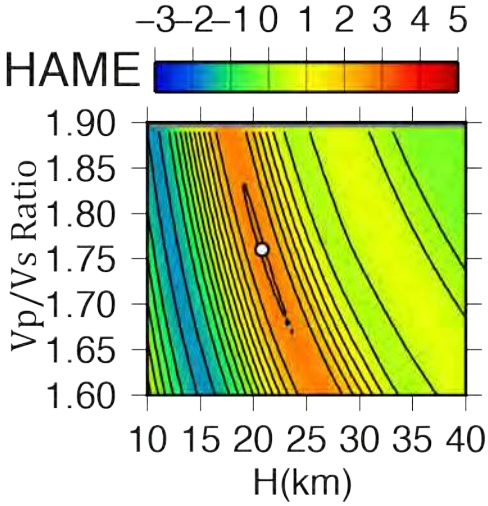
HAME
–3 –2 –1 0 1 2 3 4 5
Vp/Vs Ratio
1.90
1.85
1.80
1.75
1.70
1.65
1.60
10 15 20 25 30 35 40
H(km)

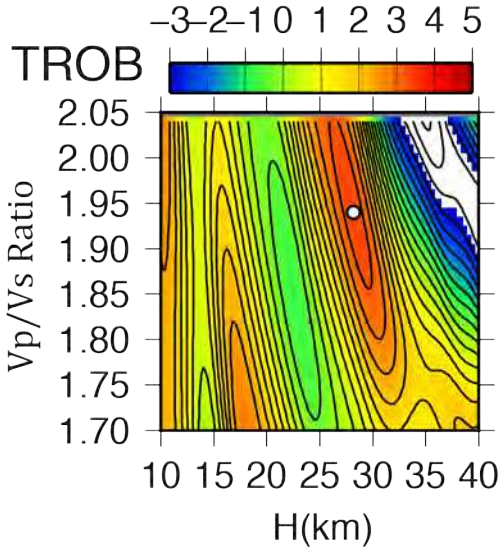
TROB
–3 –2 –1 0 1 2 3 4 5
Vp/Vs Ratio
2.05
2.00
1.95
1.90
1.85
1.80
1.75
1.70
10 15 20 25 30 35 40
H(km)

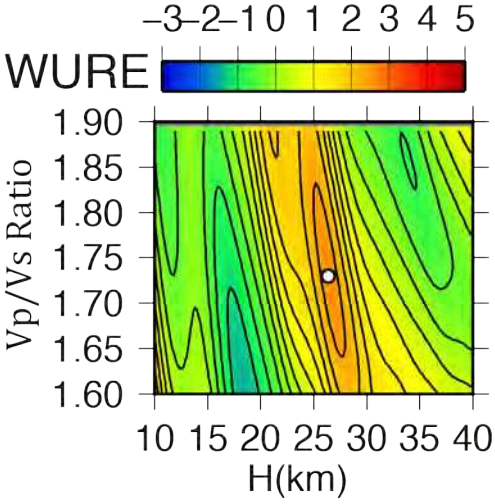
WURE
–3 –2 –1 0 1 2 3 4 5
Vp/Vs Ratio
1.90
1.85
1.80
1.75
1.70
1.65
1.60
10 15 20 25 30 35 40
H(km)

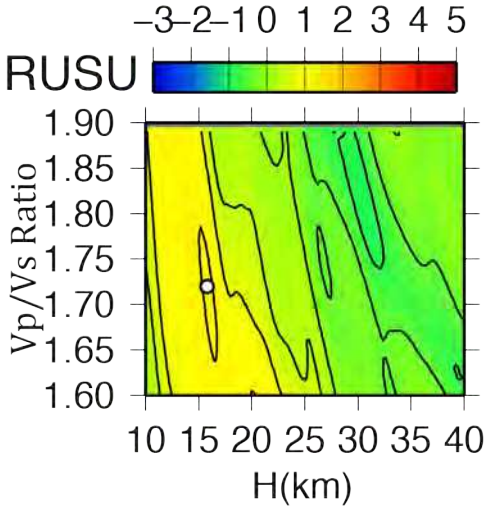
RUSU
–3 –2 –1 0 1 2 3 4 5
Vp/Vs Ratio
1.90
1.85
1.80
1.75
1.70
1.65
1.60
10 15 20 25 30 35 40
H(km)

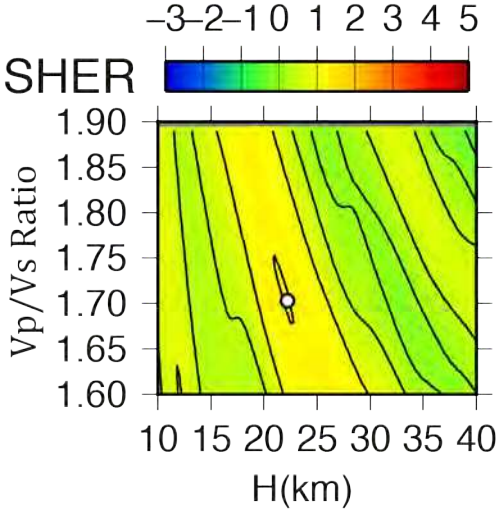
SHER
–3 –2 –1 0 1 2 3 4 5
Vp/Vs Ratio
1.90
1.85
1.80
1.75
1.70
1.65
1.60
10 15 20 25 30 35 40
H(km)

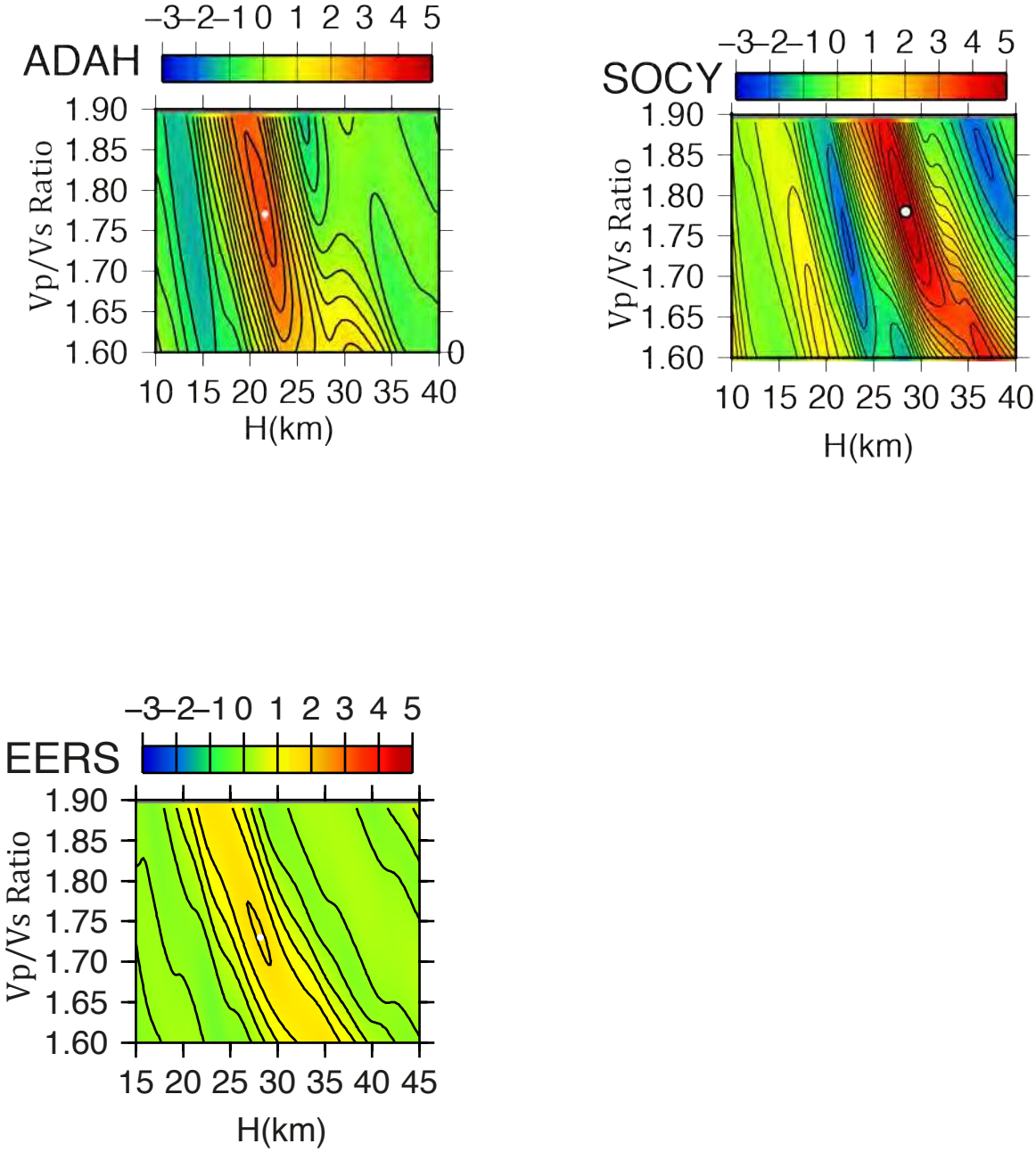


**Figure S2:**

Crustal thickness (H) versus Vp/Vs ratio diagrams from the H-k stacking method for the 21 stacked receiver functions shown in Figure S1. The maximum of the stacking amplitude is indicated by the white point and corresponds to the value indicated in Tab. 1.

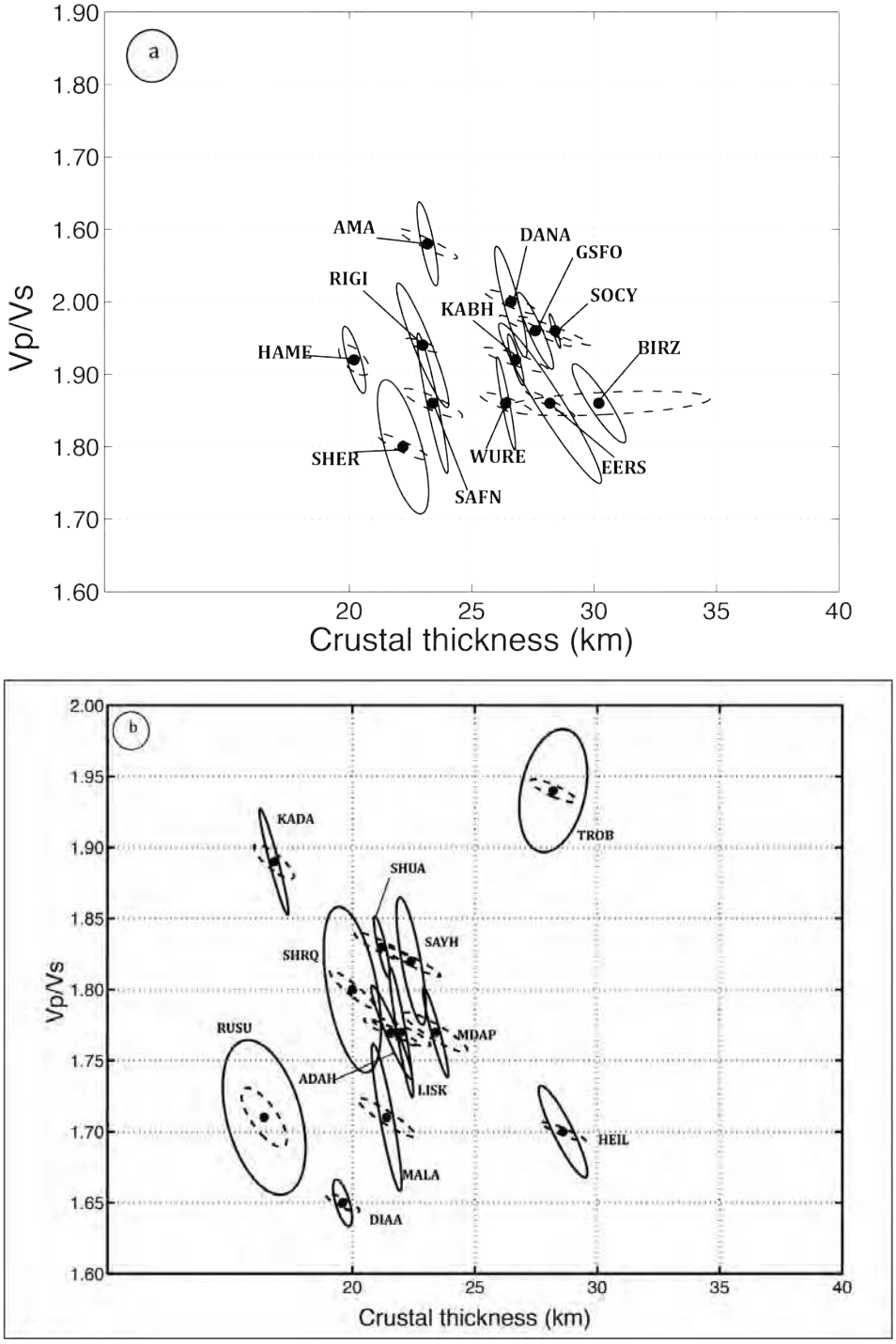


**Figure S3:**

Solid lines are Vp/Vs as a function of crustal thickness H with bootstrap error estimates for the stacking method and dashed lines are from the initial velocity model for the stations located parallel to the northern coast in (a) and parallel to southern coast in (b).

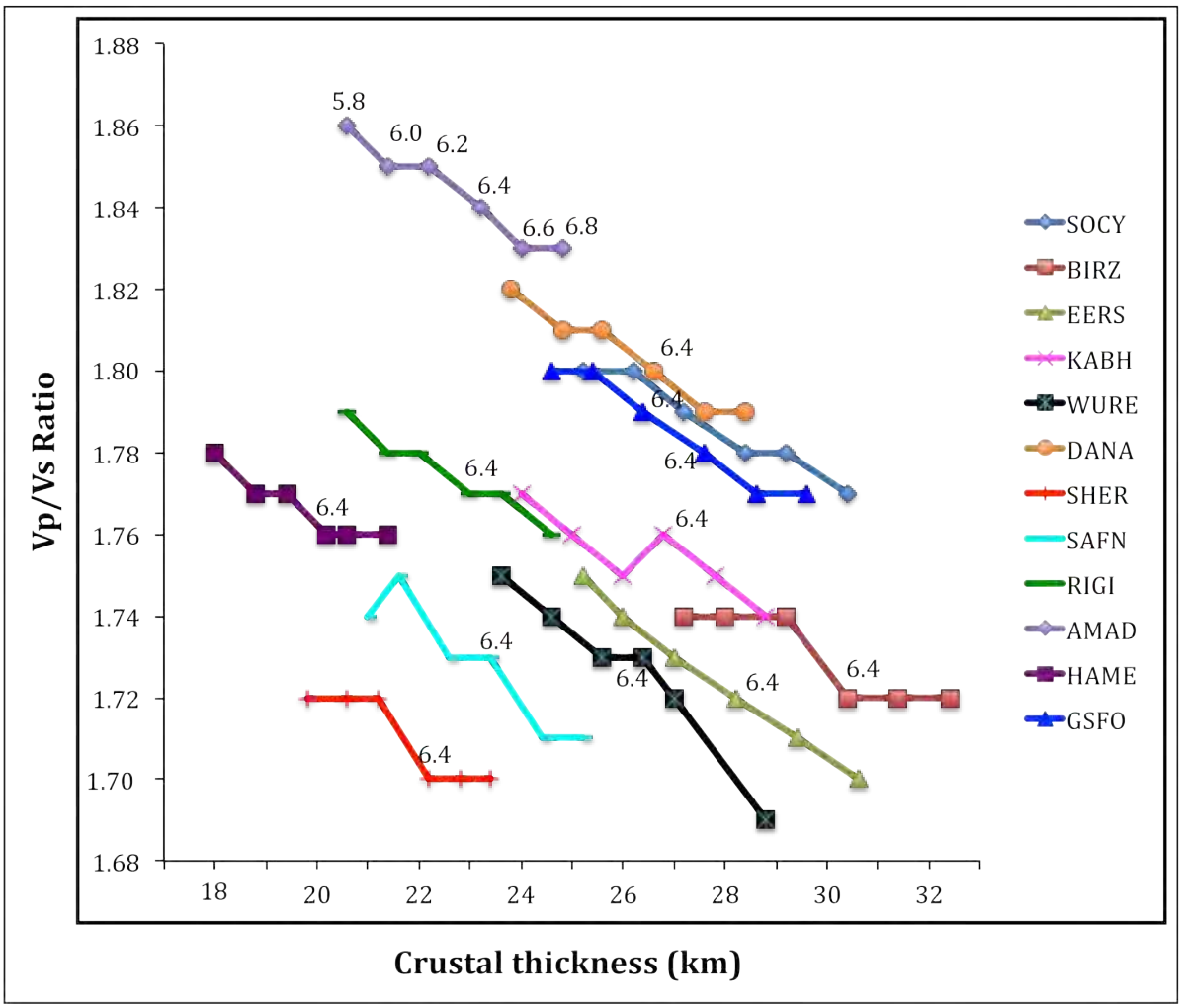


**Figure S4:**

An example of the inverted H-k values using different average crustal velocity Vp in the range 5.8 - 6.8 km/s with 0.2 km/s step.